Heart of Entanglement: Chiral, Nematic, and Incommensurate Phases in the Kitaev-Gamma Ladder in a Field

Erik S. Sørensen,[1,*] Andrei Catuneanu,[2] Jacob S. Gordon,[2] and Hae-Young Kee[2,3,†]

[1]*Department of Physics, McMaster University, Hamilton, Ontario L8S 4M1, Canada*
[2]*Department of Physics, University of Toronto, Toronto, Ontario M5S 1A7, Canada*
[3]*Canadian Institute for Advanced Research, CIFAR Program in Quantum Materials, Toronto, Ontario M5G 1M1, Canada*

(Received 5 June 2020; revised 24 November 2020; accepted 4 December 2020; published 21 January 2021)

The bond-dependent Kitaev model on the honeycomb lattice with anyonic excitations has recently attracted considerable attention. However, in solid-state materials other spin interactions are present, and among such additional interactions, the off-diagonal symmetric Gamma interaction, another type of bond-dependent term, has been particularly challenging to fully understand. A minimal Kitaev-Gamma model has been investigated by various numerical techniques under a magnetic field, but definite conclusions about field-induced spin liquids remain elusive. One reason for this may lie in the limited sizes of the two-dimensional geometry it is possible to access numerically, and missed incommensurately ordered states may be interpreted as a spin liquid. Here we focus on the Kitaev-Gamma ladder model as a guide to the phase space of disordered states which could potentially become a spin liquid in the two-dimensional limit. We determine the entire phase diagram in the presence of a magnetic field along the [111] direction. Because of the competition between the interactions and the field, an extremely rich phase diagram emerges with 15 distinct phases. Focusing near the antiferromagnetic Kitaev region, we identify nine different phases solely within this region: several incommensurate magnetically ordered phases, spin-nematic, and *two* chiral phases with enhanced entanglement. Of particular interest is a highly entangled phase with *staggered chirality* with zero-net flux occurring at intermediate field, which along with its companion phases outlines a heart-shaped region of high entanglement, the heart of entanglement. We compare our results for the ladder with a C_3 symmetric cluster of the two-dimensional honeycomb lattice, and offer insight into possible spin liquids in the two-dimensional limit.

DOI: 10.1103/PhysRevX.11.011013

Subject Areas: Condensed Matter Physics, Magnetism, Strongly Correlated Materials

I. INTRODUCTION

The Kitaev model on a two-dimensional honeycomb lattice is a rare example of an exactly solvable model offering a quantum spin liquid with fractional excitations [1]. Under a time-reversal symmetry breaking field, it exhibits non-Abelian anyons with half-quantized thermal Hall conductivity originated from Majorana edge mode. Since the original proposal, finding a solid-state material possessing such a quantum spin liquid has attracted great attention. A microscopic mechanism for realizing the Kitaev model in solid-state material was first suggested using the combined effects of strong spin-orbit coupling and electron-electron interactions [2,3]. Later, the nearest neighbor generic spin model on an ideal honeycomb lattice was rederived, and it was found that there are additional bond-dependent interactions present, with the so-called Gamma (Γ) interaction among the most intriguing [4].

From the material perspective, α-$RuCl_3$ was proposed as a leading candidate with a weaker coupling between layers making the material close to two dimensional (2D) [5–10]. Furthermore, the Γ interaction has been found to be as large as the Kitaev interaction in α-$RuCl_3$ [11–13]. Since then, $RuCl_3$ has been explored by several experimental and theoretical techniques [14–18]. In particular, early inelastic neutron scattering [10] and Raman spectroscopy [19] measurements have suggested a strong frustration well above the magnetic ordering temperature, indicating strong frustration which may originate from the bond-dependent Kitaev and Γ interactions. Remarkably, a half-quantized thermal Hall conductivity was recently reported in α-$RuCl_3$ in a certain range of the magnetic field [20] when a zigzag

*sorensen@mcmaster.ca
†hykee@physics.utoronto.ca

magnetically ordered phase is destroyed by the magnetic field [21]. Other physical quantities accessed by several experimental techniques in $RuCl_3$ also suggested that there is a nontrivial intermediate phase under a magnetic field which is different from a trivially polarized spin state in high field regime [22–31]. However, the experimental evidence for a field-induced intermediate disordered phase in $RuCl_3$ is still under debate [32–34].

In parallel to the experimental progress, theoretical attempts to find nontrivial field-induced phases in extended Kitaev model have been pursued extensively [12,35–48]. Most numerical studies are limited to either near the antiferromagnetic (AFM) Kitaev or near the ferromagnetic (FM) Kitaev region, as the exactly solvable Kitaev point offers a starting point. In particular, a minimal Kitaev-Gamma (KG) model under a [111] magnetic field has been studied near a FM Kitaev and a AFM Γ region relevant to $RuCl_3$ [46–49]. A 24-site exact diagonalization (ED) study showed a field-revealed Kitaev spin liquid near the FM Kitaev region with a finite AFM Γ interaction, when the magnetic field is tilted away from the [111] axis [49]. However, the infinite tensor product state found a small confined Kitaev spin liquid, and broken C_3 rotational phases are induced under the magnetic field [47]. Interestingly, various large unit cell magnetic orderings have been reported in the classical KG model under the magnetic field along the [111] axis [46], which are replaced by these broken rotational phases in the quantum model [48]. Whether the C_3 broken phases are quantum spin liquids or not is at present not clear and will require further studies.

Numerical studies near the AFM Kitaev (AK) limit under a magnetic field have found intriguing results [37,39–42,45,50–52]. It was suggested that a gapless U(1) spin liquid is induced by the magnetic field [45]. The energy spectra obtained by 24-site ED showed putative gapless excitations in the intermediate field, which then transition to a polarized state (PS) in the high field regime. Several infinite density matrix renormalization group (iDMRG) studies also reported a change of central charge depending on the number of legs in the DMRG which indicates a finite spinon Fermi surface [50]. However, one may question if the dense energy spectra are due to incommensurate order which is difficult to detect due to the finite size of ED and limited access to momentum points in iDMRG. Indeed, different iDMRG studies have found different gapless points in momentum space [39,50,52].

Despite intensive studies, definite conclusions on possible phases and the nature of numerically determined phases near the Kitaev regions remain indefinite. One reason for the controversial results among the previous studies may lie in the limited sizes of the two-dimensional honeycomb geometry that one can access numerically. Furthermore, the zero-field and field-induced phases of the entire phase space of the KG model are yet to be determined. We therefore focus on the KG model defined on a two-leg ladder which is much more amenable to a detailed study and a complete phase diagram in the presence of a magnetic field along the [111] direction can be determined. Using high throughput iDMRG calculations we map out the entire phase diagram of the KG ladder which shows an extremely rich structure. After we determine the entire phase diagram, we focus on the region of the phase diagram where the Kitaev interaction is predominantly AFM. In this region, in the absence of a magnetic field, we identify a novel spin-nematic (SN) phase with quadropolar order in addition to the AFM Kitaev phase (AK) and a phase connected to the isotropic FM ladder through a local six-site spin rotation, FM_{U_6} [53–56]. In zero field the KG ladder can be mapped to a ladder with four-spin exchange closely related to JQ models [57] (Heisenberg models with four-spin interactions) extensively studied as models of deconfined criticality [58].

When a magnetic field in the [111] direction is introduced, field and spin interactions compete, and a proliferation of phases is observed. We identify phases with scalar chiral ordering and several phases with magnetic ordering, some of which might display incommensurate or very large unit cell ordering. Of particular interest is two chiral ordered phases characterized by a staggered chirality (SC) and uniform chirality (UC). The SC phase is a magnetically disordered and highly entangled phase occurring at intermediate magnetic field above the AK phase. It has the staggered chirality with zero-net flux despite it is under a rather large external field, and shows clear chain end excitations. Rather poetically, this phase along with its companion phases outline a heart-shaped region of high entanglement, "the chiral heart of entanglement." On the other hand, the UC phase with the uniform chirality leading to a finite net flux appears between the SN and the rung singlet (RS_{U_6}) phase connected to the isotropic AFM ladder through a local six-site spin rotation [53–56]. It emerges at extremely low field, as if three phases, SN, UC, and RS_{U_6}, may meet at a critical point. All together, near the AFM Kitaev region alone, we identify 9 possible distinct phases in addition to the FM_{U_6} phase and the PS occurring at high magnetic fields. Including phases away from the AFM Kitaev region, we identify a total of 15 phases shown in Figs. 2, 4, and 5 and elsewhere. Before we discuss these phases in detail in the following sections, we summarize their assigned names, their description, and reference in the Table I.

In Sec. II, we first review the KG model. In addition to the extensive 2D cluster studies, a one-dimensional (1D) KG chain model including only x and y bonds was studied using non-Abelian bosonization and DMRG and reported SU(2) emergent phases [59]. The two-leg ladder is made of two such KG chains by connecting them by the z bond. Technical details relevant to the iDMRG and DMRG numerical methods are subsequently discussed in Sec. III.

TABLE I. Abbreviation of the 15 phases found in the two-leg KG ladder model under a [111] field as shown in Figs. 2, 4, and 5. Their description and corresponding section are listed. Some phases include special points along with their description.

Phase	Description	Section
SC	Staggered chirality without a magnetic order	V A, V B
UC	Uniform chirality without a magnetic order	V A, V B
AK	Disordered with string order; AFM Kitaev point	V A, V C
FM_{U_6}	Magnetic order; FM SU(2) Heisenberg point	IV A
RS_{U_6}	Magnetic order; AFM SU(2) Heisenberg point	IV A
SN	Spin-nematic phase with two magnetic orderings	IV A 1
FK	Disordered with string order; FM Kitaev point	IV A
AΓ	Disordered; AFM Γ point	IV A
ZZ	Zigzag magnetic phase	IV A
PS	Polarized state	IV C
η	Incommensurate	V A 1
β	Incommensurate or large unit cell	V A 1
τ	Incommensurate or large unit cell	V A 1
γ	Large unit cell	V A 1
μ	Incommensurate or large unit cell	V A 1

An overview and detailed discussion of the full phase diagram of the ladder is presented in Sec. IV along with a discussion of the connection between the KG chain and the ladder. In Sec. V, we focus on the vicinity of the AFM Kitaev region under a magnetic field, where a rich phase diagram with various phases with enhanced entanglement is found. Finally, in Sec. VI we compare our results for the ladder with 24-site ED results obtained in the honeycomb geometry and discuss the implications of the ladder results to the 2D limit.

II. TWO-LEG KITAEV-GAMMA LADDER

The two-leg KG ladder is formed out of a strip of the honeycomb lattice. The two KG chains with only x and y bonds are coupled by adding the z bond as shown in Fig. 1. Periodic boundary conditions in the direction perpendicular to the ladder are then imposed by directly coupling the dangling z bonds thereby forming a regular ladder. These

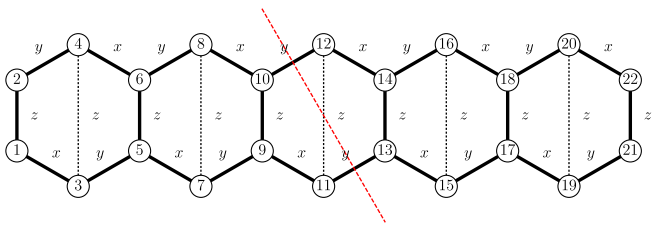

FIG. 1. Two-leg ladder KG honeycomb strip with alternating x and y bonds along the leg and z bond between the chains with the numbering of the sites used throughout the paper. The dashed red line indicates the partition used for $\rho_{N/2-1}$.

z bonds are shown as dotted vertical bonds in Fig. 1. Sometimes the additional z bonds from imposing periodic boundary conditions are taken to be of opposite sign (and/or strength), in which case the resulting model is usually referred to as a honeycomb ladder [60]. Here, all z bonds are identical and a regular ladder is formed. In addition to the bond-dependent Kitaev interaction, the KG Hamiltonian incorporates another bond-dependent interaction Γ [4]. For the KG ladder we orient the bonds so that the Kitaev z bond connects the two legs of the ladder as shown in Fig. 1. The complete Hamiltonian is then given by

$$H_{\mathrm{KG}} = \sum_{\langle i,j\rangle_{\gamma\in(x,y,z)}} K S_i^\gamma S_j^\gamma + \Gamma(S_i^\alpha S_j^\beta + S_i^\beta S_j^\alpha), \qquad (1)$$

where (α,β) takes on the values $(y,z)/(x,z)/(x,y)$ for $\gamma = x/y/z$, and $\langle i,j\rangle$ refers to the nearest neighbor sites. We keep $K = \cos\phi$ and $\Gamma = \sin\phi$ and interpolate between the Kitaev ladder and Γ ladder by varying ϕ from 0 to 2π. We denote the total number of sites in the ladder (including both legs) by N. The pure Kitaev ladder at $\phi = 0, \pi$ is exactly solvable [61] and at both points it is in a disordered gapped phase [61]. However, recently it was shown that a nonlocal string order parameter (SOP) can be defined [62] at the Kitaev points. The SOP remains nonzero in the presence of a small Heisenberg coupling J at both the Kitaev points. Close to the FM Kitaev point, $\phi = \pi$, the phase diagram of the KG ladder has recently been investigated in the presence of a magnetic field and additional interactions [49]. On the other hand, relatively little is known about the rest of the phase diagram of the KG ladder which is our focus here.

In one dimension in the absence of a magnetic field, the closely related KG chain has been investigated in considerable detail [59,63]. An extended disordered phase close to the AFM Kitaev point, $\phi = 0$, has been identified along with an adjacent spin-nematic phase. For the KG chain it can rigorously be established that the phase diagram is symmetric with respect to $\Gamma \to -\Gamma$, a symmetry that is clearly absent in the KG ladder.

It is of particular interest to also consider the effect of a magnetic field. Here we exclusively consider a field in the [111] direction, perpendicular to the honeycomb plane of the ladder. The magnetic field leads to a Zeeman coupling as

$$H = H_{\mathrm{KG}} - g\frac{\mu_B}{\hbar}\sum_i \mathbf{h}\cdot\mathbf{S}, \qquad (2)$$

where we choose the direction of $\mathbf{h}$ along the [111] axis normalized as $\mathbf{h} = (h/\sqrt{3})(1,1,1)$, $g = 1$, and $\mathbf{S} = \hbar(\sigma/2)$ where σ is a Pauli matrix. We use units with $\hbar = 1$ and $\mu_B = 1$.

III. NUMERICAL METHODS

As our main tools for investigating the KG ladder, we use exact diagonalization, finite-size density matrix renormalization group [64–69], and infinite DMRG [69,70] techniques. The iDMRG calculations are performed in two different ways. A high throughput mode with a small unit cell of size 24 or 60 and a maximal bond dimension of 500 and a high precision mode with a unit cell of 60 and a maximal bond dimension of 1000. Typical precisions for the two iDMRG modes are $\epsilon = 10^{-8}$ and $\epsilon = 10^{-10}$, respectively, and $\epsilon = 10^{-10}$ for the finite-size DMRG calculations. Finite-size DMRG calculations are performed both with open boundary conditions (OBC) and for smaller system sizes with periodic boundary conditions. In order to establish the phase diagram we focus on several different characteristics. With e_0 the ground-state energy per spin, we define the energy susceptibilities,

$$\chi_h^e = -\frac{\partial^2 e_0}{\partial h^2}, \qquad \chi_\phi^e = -\frac{\partial^2 e_0}{\partial \phi^2}, \tag{3}$$

where χ_h^e could equally well be called a magnetic susceptibility. For finite-size systems of size N it has been established [71] that the energy susceptibility at a quantum critical point (QCP) diverges as

$$\chi^e \sim N^{2/\nu - d - z}. \tag{4}$$

Here ν and z are the correlation and dynamical critical exponents and d is the dimension. It follows that χ^e may not necessarily detect the phase transition if the critical exponent ν is sufficiently large. We have therefore found it useful to supplement the analysis of χ^e by a study of the entanglement spectrum [72] at different sections of the ladder. We have found it most useful to use a partition of the ladder where a cut is introduced at site $N/2 - 1$ thereby intersecting a rung (see Fig. 1). With λ_α the eigenvalues of the resulting reduced density matrix, $\rho_{N/2-1}$ the entanglement spectrum can be defined as $-\ln \lambda_\alpha$ and yields a characteristic signature of a phase. Close to the QCP the λ_α rapidly change whereas they remain approximately constant inside a phase. We therefore focus on the largest of the λ_α's which we denote by λ_1 and study the lowest edge of the entanglement spectrum defined by

$$-\ln \lambda_1. \tag{5}$$

This quantity is often called the single copy entanglement [73] in a quantum information context. In a product phase $\lambda_1 = 1$ ($-\ln \lambda_1 = 0$) and such phases, with zero entanglement, are therefore easily detected by tracing out $-\ln \lambda_1$. Conversely, phases with high entanglement will have $-\ln \lambda_1 \gg 0$, and of course, due to the ordering of the λ_α one must have $-\ln \lambda_\alpha > -\ln \lambda_1$ for any $\alpha > 1$. Sometimes changes in $-\ln \lambda_1$ are imperceptible and we have therefore found it useful to define an entanglement spectrum susceptibility (or single copy entanglement susceptibility) as follows:

$$\chi_h^{\lambda_1} = -\frac{\partial^2 \lambda_1}{\partial h^2}, \qquad \chi_\phi^{\lambda_1} = -\frac{\partial^2 \lambda_1}{\partial \phi^2}. \tag{6}$$

Since the entanglement spectrum *has* to change at the QCP, χ^{λ_1} should be able to detect *any* phase transition with the exception of unlikely scenario's where λ_1 only changes linearly at the QCP with all nontrivial changes in the higher λ_α's. We have found χ^{λ_1} to be an *extremely* sensitive measure, often changing many orders of magnitude at a QCP, and we therefore typically focus on $\ln \chi^{\lambda_1}$.

IV. FULL KG LADDER ϕ,$h[111]$ PHASE DIAGRAM

We start with a discussion of the full phase diagram covering the entire range $\phi \in [0, 2\pi]$ and $h[111] \in [0, 1.75]$. Our results for the full phase diagram as obtained from iDMRG calculations are shown in Fig. 2. We first show $\ln \chi_\phi^{\lambda_1}$ in Fig. 2(a). The divergence of $\chi_\phi^{\lambda_1}$ at a phase transition is so strong that it is most sensible to plot $\ln \chi_\phi^{\lambda_1}$. A well-defined phase, where λ_1 is close to constant, is then visible in Fig. 2(a) as a dark blue coloring. On the other hand, a divergent $\chi_\phi^{\lambda_1}$, indicating a phase transition is visible as a dark red color. As is clearly evident from Fig. 2(a) the complexity of the phase diagram due to the many competing phases is truly remarkable.

Figures 2(b) and 2(c) show χ_ϕ^e and $-\ln \lambda_1$, and the spin excitation gap at zero field, respectively. We discuss them in detail later.

A second view of the full phase diagram is shown in Fig. 2(d) where the bipartite von Neumann entanglement entropy S_{rung} is shown. We define

$$S_{\text{rung}} = -\text{Tr} \rho_{N/2-1} \ln \rho_{N/2-1}, \tag{7}$$

where $\rho_{N/2-1}$ is the reduced density matrix obtained from a partition of the ladder after site $N/2 - 1$, a partition that will cut a *rung* in the ladder. The partition is indicated in Fig. 1. Highly entangled phases are visible as bright yellow colors, whereas phases with negligible or no entanglement, i.e., the ground-state wave function is described by a simple product form, are shown as dark blue colors.

We note that considerable scattering is clearly visible in certain regions at finite fields, for instance, above $\phi = \pi/4$ and $\phi = 0$. The noise is due to poor convergence of the iDMRG due to the high frustration present. In these regions a more careful analysis with either exact diagonalizaiton or finite-size DMRG is necessary.

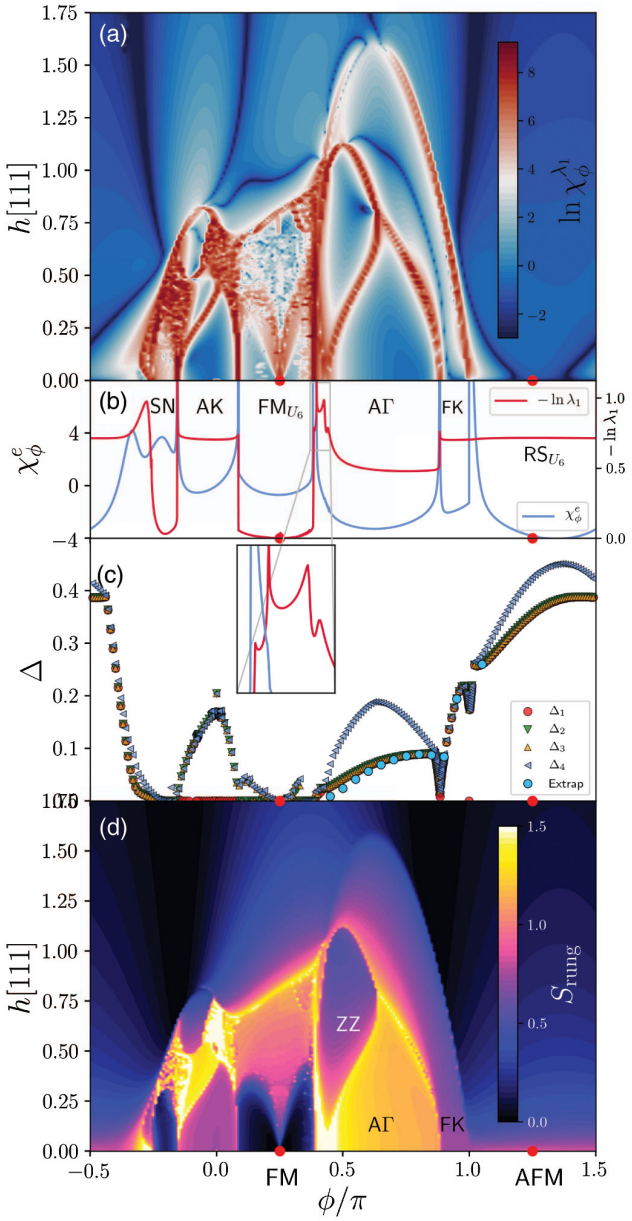

FIG. 2. Phase diagram of the two-leg KG ladder model versus field, $h[111]$, and coupling ϕ/π. (a) The entanglement spectrum susceptibility $\chi^{\lambda_1}_\phi$ on a logarithmic scale. (b) The energy susceptibility, χ^e_ϕ (blue line) versus ϕ in zero field, and the single copy entanglement, $-\ln\lambda_1$ (red line), versus ϕ in zero field. (c) The excitation gap to the first four states; solid blue circles are extrapolations of Δ_1 to $N=\infty$. (d) $S_{\rm rung}$ versus ϕ and $h[111]$. See labels in Fig. 4. Results in (a) and (d) are from high throughput iDMRG calculations with a unit cell of 60 sites with $\Delta\phi=0.01\pi$, $\Delta h[111]=0.01$. Results in (b) are from high precision iDMRG calculations with a unit cell of 60 sites with $\Delta\phi=0.001\pi$. Results in (c) are from high precision finite-size DMRG calculations with periodic boundary conditions, $N=60$, and $\Delta\phi=0.01\pi$. Close to $\phi=\pi$ and $\phi=0.88\pi$, $\Delta\phi=0.001\pi$.

A. Zero-field phase diagram

Let us now focus on the phase diagram in zero field. A detailed high precision calculation of χ^e_ϕ at zero field is shown in Fig. 2(b) along with the lower edge of the entanglement spectrum, $-\ln\lambda_1$ (the single copy entanglement). A large number of well-defined phase transitions are clearly visible, which we now discuss.

Part of the phase diagram close to the FM Kitaev point, $\phi=\pi$, has previously been discussed [49], and in zero field a gapped spin-liquid phase denoted KSL between $\phi/\pi=1$ and $\phi/\pi=0.883$ along with a second gapped phase KΓSL starting below $\phi/\pi=0.883$ have been identified. Since we here discuss the full phase diagram, we shall refer to the KSL phase as FK and the KΓSL phase as AΓ to distinguish them from the phases occurring at the AFM Kitaev point. The notation AΓ makes sense since this phase surrounds $\phi=\pi/2$, where $K=0$, $\Gamma=1$.

A *local* unitary transformation U_6 is also known [59,63,74]. The U_6 transformation locally rotates the spins in a manner so that the Γ couplings are transformed into Heisenberg-like (xx, yy, or zz) couplings with a changed sign. The transformation can be applied equally well to the chain, the ladder, and the honeycomb plane. At the points $\phi=\pi/4$ and $\phi=5\pi/4$, where the Kitaev and Γ couplings are of equal strength, the KG ladder is therefore transformed into an isotropic FM and AFM Heisenberg ladder. These two points therefore have hidden SU(2) symmetry. It is well established that the isotropic AFM Heisenberg ladder is in a gapped disordered rung singlet phase [75,76] and we therefore denote the corresponding phase for the KG ladder as RS$_{U_6}$. In the two-dimensional honeycomb lattice limit the RS$_{U_6}$ phase becomes a 120° ordered phase [4]. For the FM point, $\phi=\pi/4$, we denote the magnetically ordered gapless phase by FM$_{U_6}$. Since the FM$_{U_6}$ is well approximated by a product wave function with negligible entanglement, it is distinctly visible in Fig. 2(d) with its almost black coloring. The FM and AFM points are shown as solid red circles along the ϕ axis in Fig. 2. The same unitary U_6 transformation transforms the FM Kitaev point, $\phi=\pi$, to the AFM Kitaev point, $\phi=0$. The energy spectrum at these two points must therefore be identical, a property that does not hold for any nonzero Γ.

Starting from right to left we observe that the transition from RS$_{U_6}$ to the FK phase occurs at $\phi/\pi=1$ with the subsequent transition from the FK phase to the AΓ phase occurring at $\phi/\pi=0.883$. Between the gapless FM$_{U_6}$ phase and the gapped AΓ phase we observe a rapid sequence of several well-defined phase transitions at $\phi/\pi=0.440$, $\phi/\pi=0.428$, $\phi/\pi=0.396$, and finally at $\phi/\pi=0.385$. See enlargement shown as inset in Fig. 2(c). While χ^e_ϕ only detects a single transition at $\phi/\pi=0.385$, the other three transitions are clearly identifiable in $-\ln\lambda_1$,

as shown in the enlarged inset. The precise nature of the intervening phase is at present unclear and left for future study. A clear transition out of the FM_{U_6} phase to the gapped spin-liquid phase AK is observed at $\phi/\pi = 0.086$. As previously mentioned, precisely at $\phi = 0$ a nonlocal string order has been found [62] and the AK phase is clearly identifiable as a spin-liquid phase. In the 2D honeycomb lattice limit the AK phase becomes the AFM Kitaev spin liquid. We discuss the AK phase further below. We now turn to a discussion of the last phase observed in zero field, to the left of the AK phase.

1. Nematic phase in zero field, SN

In a recent study [63] the KG chain was investigated and a phase with spin-nematic (spin-quadropole) order adjacent to the spin-liquid phase at $\phi = 0$ was identified. From a symmetry analysis of the following four order parameters were identified:

$$\begin{aligned} Q_c &= S^x_j S^y_{j+1} + S^y_j S^x_{j+1}, \\ Q_d &= S^y_{2n+1} S^z_{2n+2} + S^z_{2n+1} S^y_{2n+2} \\ &\quad + S^x_{2n+2} S^z_{2n+3} + S^z_{2n+2} S^x_{2n+3}, \quad n = 0, 1, \ldots, \\ Q_e &= S^y_{2n+1} S^y_{2n+2} + S^x_{2n+2} S^x_{2n+3}, \quad n = 0, 1, \ldots, \\ Q_f &= S^z_j S^z_{j+1}. \end{aligned} \tag{8}$$

The two order parameters Q_c and Q_d describe off-diagonal ordering between sites not coupled by the same terms in the Hamiltonian and Q_e, Q_f diagonal ordering again between sites not coupled the same way in the Hamiltonian. The above definitions therefore depend on a specific ordering of the couplings along the leg. In Eq. (8) we only consider a single leg of the ladder and, as opposed to the rest of the paper, we number the sites on the leg consecutively, $1, 2, 3\ldots$. Considering only the Kitaev coupling, site 1, 2 would be xx coupled, site 2, 3 yy coupled, and so forth. (Note that along the legs of the KG ladder no $S^z S^z$ coupling occurs so Q_f and Q_c can be defined between any two nearest neighbor sites.) We can then use the same order parameters to study nematic ordering along the legs of the KG ladder. Our results are shown in Fig. 3 as obtained from iDMRG. Because of the translational invariance the Q's are the same among all sites and are easily calculated. They all four become nonzero at $\phi/\pi = -0.155$, which coincides with divergences in χ^e_ϕ and $\chi^{\lambda_1}_\phi$. The transition by varying ϕ is also clearly visible directly in $-\ln\lambda_1$, as can be seen in Fig. 2(b).

However, this is not a conventional spin-quadropole phase. The DRMG with OBC shows two different magnetic orderings depending on the size of the system. One has the AFM order along the leg and FM between the rung, and the other has a six-site ordering mapping to AFM order after six-site transformation, while the iDMRG finds the first one. The AFM order corresponds to a stripe order, if we continue the ordering pattern by increasing the number of ladders to the 2D limit. Let us briefly consider what happens if an additional Heisenberg coupling J is introduced alongside the K and Γ terms. In that case, the striped phase appears for an AFM Heisenberg interaction $J > 0$ in 24-site ED calculations on the C_3 cluster, while the second ordering is likely a spiral order occurring for $J < 0$ [4]. This suggests that this particular window of ϕ with $J = 0$ is in fact a line of first order transitions (in J) between these two orderings. To confirm such a possibility, we have studied the phase boundary by sweeping J (parametrized as $J \equiv K\cos\theta$). Indeed, we find a clear first order transition occurring at $J = 0$ in χ^e_θ, the second derivative of ground-state energy per spin with respect to θ, as shown Appendix A.

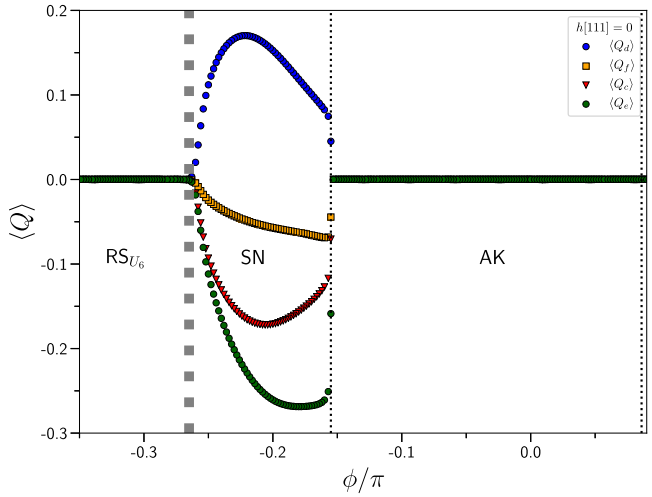

FIG. 3. Nematic ordering at zero field in the AFM Kitaev region. The nematic order parameters are determined along *one* leg of the KG ladder. Results are from high precision iDMRG calculations with a unit cell of 60, calculated in the $J \to 0^+$ limit with a small Heisenberg coupling J. The dotted vertical lines denote the transitions at critical fields determined from divergences in χ^e_ϕ and $\chi^{\lambda_1}_\phi$.

While it is a line of first order transitions, we would refer to this as SN for spin nematic, as the SN is a common feature of these orderings coexiting along the transition line. As the magnetic field becomes finite, it develops a magnetic order with almost zero entanglement, which is shown later. The transition out of the SN phase into the RS_{U_6} phase occurs at around $\phi/\pi = -0.265$. As we discuss later, this quantum phase transition is actually a multicritical point where the first order transition line ends, and two other phases occur. A high precision determination of the location of the critical point is therefore significantly more difficult than for the other QCPs. In particular so, since the entanglement for $\phi < \phi/\pi = -0.265$ is exceedingly high. It is therefore shown as a broader dashed line in Fig. 3.

2. Excitation gap in zero field

In Fig. 2(c) we show the spin excitation gap to the first 4 lowest lying states, Δ_1, Δ_2, Δ_3, and Δ_4, as obtained from high precision finite-size DMRG on ladders with $N = 60$. We have verified that finite-size effects are relatively small if not in the proximity of a QCP. This is indicated by the solid blue circles in Fig. 2(c) which indicate extrapolations to $N = \infty$ of δ_1 by fitting data for $N = 24$, 36, 48, 60, and 72 to the form $\Delta(N) = \Delta_\infty + a\exp(-N/\xi)/N$.

Starting from the right, we find that the RS_{U_6} phase, as expected, has a single ground state with a well-defined triplet excitation throughout most of the phase. The triplet excitation merges with higher lying excitations at $\phi = 1.56\pi$. Precisely at the FM Kitaev point, $\phi = \pi$, there is a level crossing leading to a clear first order transition. This is exact also for finite systems. The same holds true by symmetry at the AFM Kitaev point, $\phi = 0$. However, while the FK phase has a single ground state below a well-defined gap and $\phi = \pi$ is a transition point, in the AK phase the ground state remains double degenerate below a gap, only split by finite-size effects. The AΓ phase also has a single ground state with a well-defined triplet excitation above it. The FM_{U_6} phase is gapless, but occasionally excited state DMRG calculations get trapped in higher lying states and the gapless nature of the phase does not appear clearly in Fig. 2(c). The final phase we discuss here, the SN phase occurring between $\phi/\pi = -0.265$ and $\phi/\pi = -0.155$, is clearly gapless, as can be seen in Fig. 2(c) with all four gaps close to zero.

B. Relation to 1D KG chain

As eluded to above, the phase diagram of the ladder is closely connected to that of the KG chain and the KG model defined on the full two-dimensional honeycomb lattice.

Comparing to the phase diagram of the KG chain [59,63], a gapped FK phase appeared in the ladder, while it was gapless in the chain model. Similarly, the AK persists near the AFM Kitaev region, and it is gapped in the ladder, while it is gapless in the chain. RS_{U_6} is gapped in the ladder similar to AFM Heisenberg model, where as it was gapless in the chain. FM_{U_6} remains magnetically ordered with gapless excitations as was the case for the chain. For the chain a gapless nematic phase was identified [63] on either side of the AK phase. For the ladder a similar gapless phase, SN, occurs but this time only on one side of the AK phase. AΓ remains disordered like the chain. There is therefore a close connection between the phases identified in the KG chain, but we expect the KG ladder to be much closer to the two-dimensional honeycomb lattice and to represent most of the phases occurring in that limit although we in some cases expect phases to become gapless in the two-dimensional limit. For instance, in the KG ladder AK and FK phases are gapped and we expect these phases to become the AFM and FM Kitaev spin liquid, respectively, in the 2D limit, which are gapless.

C. Nonzero field

When a magnetic field in the [111] direction is introduced, the full $h[111]$, ϕ phase diagram is revealed as shown in Figs. 2(a) and 2(d). From the rung entanglement S_{rung} shown in Fig. 2(d), it is clear that the introduction of a field in many cases tends to *increase* the entanglement. New highly entangled phases appear until the fully field polarized state is attained where all spins are polarized along $h[111]$. We denote this polarized state by PS. Trivially, it is a product state with zero entanglement. We start by discussing the fate of the RS_{U_6} phase. This phase is adiabatically connected to the PS phase and no phase transition is observed at any nonzero field strength. This is contrary to the FM_{U_6} phase state which cannot be adiabatically connected to the PS phase. This follows from the fact that the phase is not an ordinary FM state but only related to one through the local unitary rotation U_6. An alignment of the spins along the [111] direction is therefore energetically costly. As can be seen in Figs. 2(a) and 2(d), a line of phase transitions around field strengths of $h[111] = 0.7$–1.0 occurs, signaling the transition to the PS phase. A new phase at finite field above $\phi = \pi/2$ is clearly visible. This is a gapless, magnetically ordered phase with the spins arranged in a zigzag manner, in opposite directions on the two legs of the ladder, and we refer to this phase as the ZZ phase. The fate of the phases occurring between $\phi/\pi = 0.440$ and $\phi/\pi = 0.385$ is not known and left for future study. The FK and AΓ phases survive in the presence of a magnetic field and survive up to large field strengths. The nature of these two phases in the presence of $h[111]$ has previously been discussed [49]. We therefore leave that part of the phase diagram aside and instead concentrate on the part of the phase diagram close to the AFM Kitaev point, $\phi = 0$.

In the vicinity of $\phi = 0$ it is clear from Figs. 2(a) and 2(d) that several new phases are induced by the magnetic field, in many cases with significantly increased entanglement. The nematic phase, SN, identified in zero field, survives in the presence of a nonzero field and is clearly visible in Figs. 2(a) and 2(d). However, the high throughput iDMRG calculations used in Fig. 2 are in certain regions having trouble achieving convergence, as can be seen by the noise in the figure and a precise determination of the phase diagram in the vicinity of $\phi = 0$ is difficult from the data presented in Figs. 2(a) and 2(d). We therefore focus on a high resolution study of that part of the phase diagram combined with finite-size DMRG calculations for the regions where it is not possible to achieve good convergence using iDMRG.

V. ANTIFERROMAGNETIC KITAEV REGION, $|\Gamma| \ll K$

The most exotic part of the phase diagram of the KG model under the field is the AFM Kitaev region around

$\phi = 0$ where $|\Gamma| \ll K$. In zero field we have identified the AK spin-liquid phase and the nematic phase SN. However, it is clear that there is a very fine balance among the different couplings and the presence of a magnetic field will substantially increase this competition. We therefore investigate this part of the phase diagram with extreme care. Our results are presented below.

In order to get a detailed picture of the phase diagram we have performed high throughput iDMRG calculations in the region $\phi \in [-0.35, 0.10]$ and $h[111] \in [0.00, 1.75]$ on a grid with $\Delta\phi = 0.002\pi$, $\Delta h[111] = 0.002$ using 24-site unit cells. By necessity, we have to use a relatively small unit cell and a maximal bond dimension of 500. Our results are shown in Fig. 4. In Fig. 4(a) is shown the lower edge of the entanglement spectrum (the single copy entanglement), $-\ln\lambda_1$, determined from the reduced density matrix that cuts a rung. Phases with negligible entanglement ($\lambda_1 \sim 1$) will show as dark blue whereas highly entangled phases ($\lambda_1 \ll 1$) are colored yellow to dark green. The AK phase is clearly visible as the bright yellow phase centered around $\phi = 0$, extending to nonzero fields. On the other hand, the SN phase which is close to a product state is clearly visible as dark blue. In addition to these two previously discussed phases there is a proliferation of phases occurring at higher fields. In order to more clearly identify phase transitions we show $\chi_\phi^{\lambda_1}$ in Fig. 4(b) on a logarithmic scale. Deep blue coloring in Fig. 4(b) corresponds to a stable λ_1, a well-defined phase, while dark red coloring signals rapid change in λ_1 and a likely associated phase transition. Note the logarithmic scale, where the darkest red coloring is more than 10 orders of magnitude larger than the blue colors. A significant advantage analyzing the phase diagram in the way shown in Figs. 4(a) and 4(b) is that the entanglement spectrum, and therefore also λ_1, *has* to change at a quantum phase transition.

In Fig. 4(b) many clear phase transitions are visible as dark red lines. However, there are also some extended regions with dark red coloring or noise appearing. These regions marked, η, τ, and μ in Figs. 4(a) and 4(b) are regions where the small unit cell iDMRG calculations have difficulty reaching good convergence. Likely this is due to incommensurability effects and a further investigation using finite-size DMRG or ED is warranted. From the data in Figs. 4(a) and 4(b) we identify six well-defined phases,

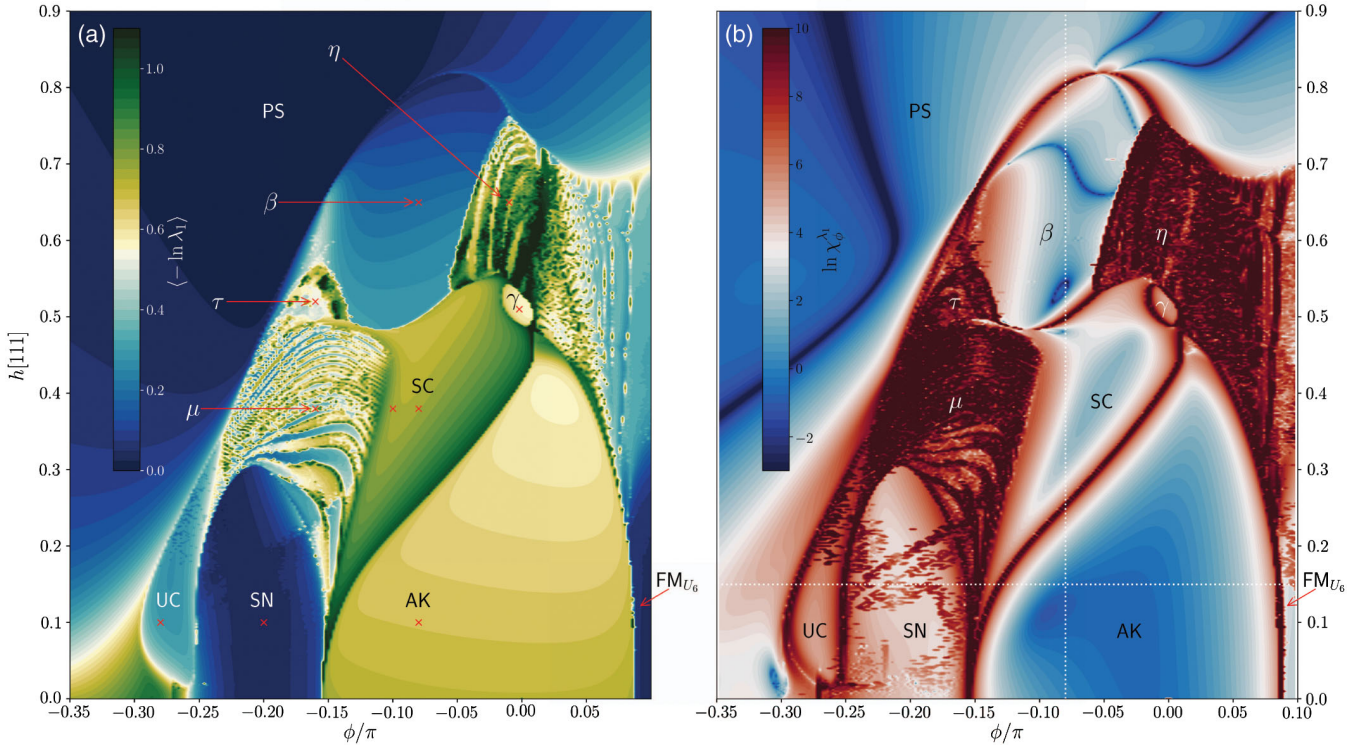

FIG. 4. Phase diagram for the AFM Kitaev region of the two-leg ladder KG ladder model under the magnetic field along [111] axis. (a) Lowest edge of the entanglement spectrum (the single copy entanglement), $-\ln\lambda_1$ of the reduced density matrix, $\rho_{N/2-1}$, versus ϕ in zero field. Dark blue corresponds to $\lambda_1 = 1 (-\ln\lambda_1 = 0)$ a phase of low entanglement and close to a product state. Dark green corresponds to a small λ_1 and higher entanglement. The $\times$'s correspond to points studied in detail in Figs. 6 and 7. (b) The entanglement spectrum susceptibility $\chi_\phi^{\lambda_1}$ on a logarithmic scale. Dark blue coloring corresponds to a stable λ_1, a well-defined phase; dark red coloring signals rapid change in λ_1 and a likely associated phase transition. The dashed lines are studied in Figs. 9 and 10. Identical phase diagrams obtained from χ_h^e and S_{rung} are shown in Fig. 5. All results in (a) and (b) are from high throughput iDMRG calculations with a unit cell of 24 sites, with $\Delta\phi = 0.002\pi$, $\Delta h[111] = 0.002$.

the previously discussed AK and SN phases and 4 new phases that we name SC, β, γ, and UC. Here, SC and UC refer staggered chirality and uniform chirality because these phases exhibit a staggered and uniform pattern of chirality without any magnetic ordering, respectively. As we discuss in more detail below, it appears that the μ region is distinct from the SC phase and it seems quite plausible that the η, τ, and μ regions are in fact well-defined phases and we therefore discuss them as such below. However, at present we cannot exclude the possibility that, for instance, what appears as a phase transition between the SN phase and the μ phase is instead a "disorder" line marking the onset of incommensurate short-range correlations thereby hindering the convergence of the iDMRG calculations. It is therefore possible that the η, τ, and μ regions are not distinct phases but simply parts of the adjoining phases where short-range correlations are different. We return to this point below. Surprisingly, it is clear that some of the phases occurring at finite field have significantly increased entanglement, most notably the SC phase that together with its accompanying phases, γ and μ, outline a heart-shaped region of extraordinary high entanglement.

Complementary views of the same phase diagram can be obtained from S_{rung} and χ_h^e as shown in Fig. 5. All the phases except for the UC phase are clearly visible in Fig. 5(a). However, the transition to the UC phase is subtle and easily missed in χ_h^e. A large precursor "bump" to this phase transition [see Fig. 10(a)] is clearly visible in the lower left-hand corner of Fig. 5(a) as the large band of bright yellow; however, this feature is not associated with any real phase transition. See also Fig. 10(a) and the surrounding discussion.

Another useful depiction of the AFM Kitaev region phase diagram can be obtained from S_{rung}, with $\rho_{N/2-1}$ the reduced density matrix of the first $N/2-1$ sites of the ladder, with the partition cutting the middle rung (and both legs) of the ladder (see Fig. 1). Our results for this quantity are shown in Fig. 5(b). In this case the UC phase along with all the other phases are clearly defined. Regions of increased values of S_{rung} are visible as bright yellow colored bands in the μ and τ phases. These bands likely describe lock-ins to particular magnetic orderings compatible with the unit cell used in the calculations. The "heart of entanglement," with its elevated entanglement, encompassing the μ, SC, and γ phases is beautifully illuminated in yellow and orange colors. Even higher bipartite entanglement is present in the η phase with its bright yellow colors.

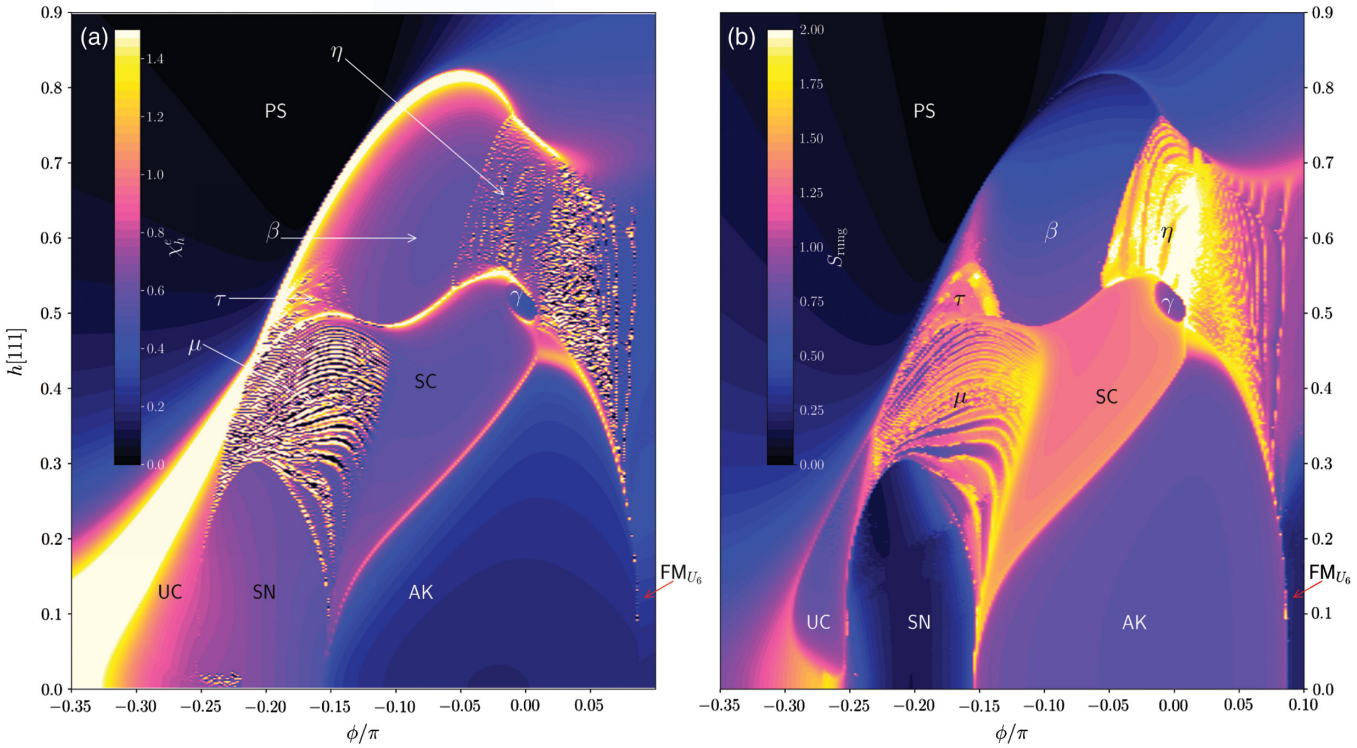

FIG. 5. (a) Phase diagram for the AFM Kitaev region of the two-leg ladder KG model under the magnetic field along [111] axis as obtained from χ_h^e. Note the absence of a clear definition of the UC phase. (b) Phase diagram for the AFM Kitaev region of the two-leg ladder KG model under the magnetic field along [111] axis as obtained from S_{rung}, the bipartite entanglement entropy at $N/2-1$. This partition cuts the middle rung of the ladder. Note the clear definition of the UC phase. All results are from high throughput iDMRG calculations with a unit cell of 24 sites, with $\Delta\phi = 0.002\pi$, $\Delta h[111] = 0.002$.

A. Overview of phases, $\langle S_i^\alpha \rangle$

Several of the phases visible in Figs. 4(a) and 4(b) are magnetically ordered phases. We have therefore performed high precision finite-size DMRG calculations with $N = 400$ and OBC at the points marked with a red $\times$ in Fig. 4(a). Results for the local magnetization $\langle S_i^\alpha \rangle$ are shown in Figs. 6 and 7; here the green circles are S_i^x, the red circles S_i^y, and the blue circles S_i^z along a *single* leg of the ladder. In some cases we find magnetic ordering with a surprisingly large unit cell, in other cases indications of incommensurate ordering. Note that a simple polarization of the spins along the field direction $h[111]$ would have all S_i^α equal. Before we present a detailed discussion of some of the phases, we summarize the main findings in Figs. 6 and 7. A summary is also provided in Table II.

1. Magnetically ordered phases

We start with the six phases that show clear signs of ordering.

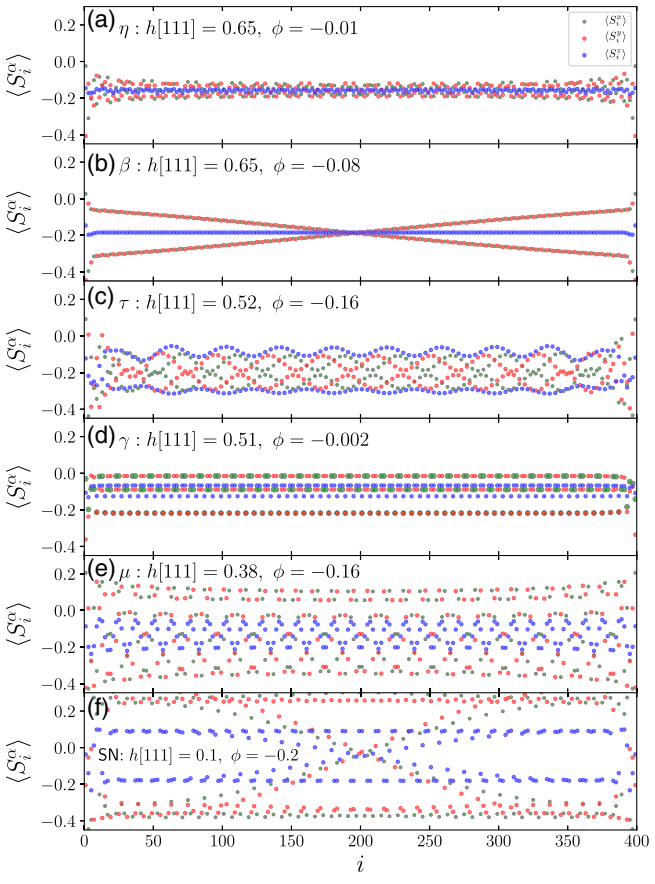

FIG. 6. On-site magnetization $\langle S_i^\alpha \rangle$, $\alpha = x$ (green), y (red), and z (blue) along the ladder at six different points in the phase diagram indicated in Fig. 2 representing the (a) η, (b) β, (c) τ, (d) γ, (e) μ, and (f) SN phases. Results are from finite-size DMRG calculations for total system size $N = 400$ with open boundary conditions. For clarity, results are shown only for *one leg* of the ladder.

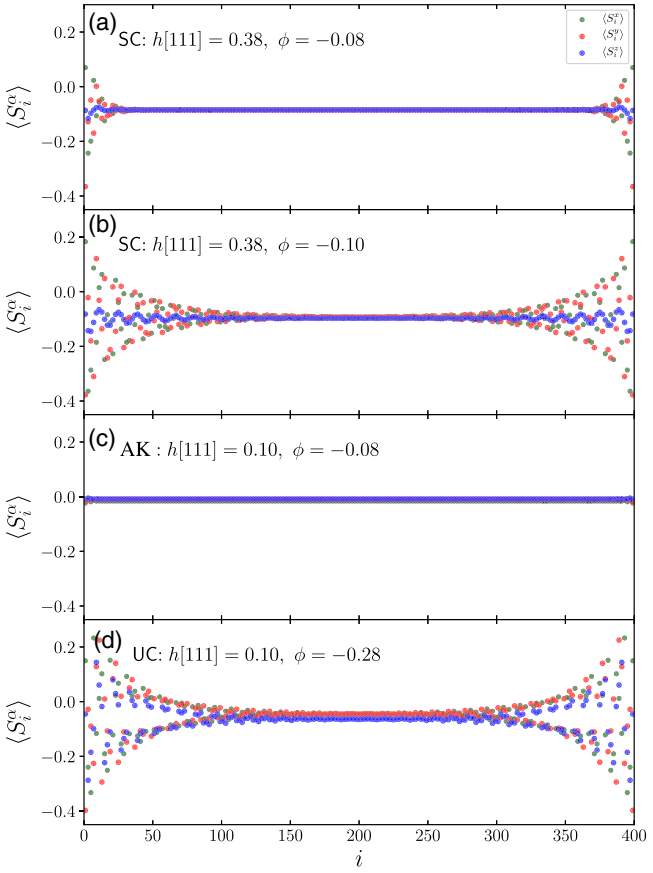

FIG. 7. On-site magnetization $\langle S_i^\alpha \rangle$, $\alpha = x$ (green), y (red), and z (blue) along the ladder at four different points in the phase diagram indicated in Fig. 2 representing the (a) SC phase at $h[111] = 0.38$, $\phi = -0.08\pi$, (b) SC phase at $h[111] = 0.38$, $\phi = -0.10\pi$, (c) AK phase and (d) UC phase. Results are from finite-size DMRG calculations for total system size $N = 400$ with open boundary conditions. For clarity, results are shown only for *one leg* of the ladder.

TABLE II. Summary of phase in the AFM Kitaev region. The magnetic ordering is in some cases with a large unit cell or incommensurate. "End excitations" refers to the presence of localized excitations at the end of the ladder.

Phase	Magnetic order	Degenerate ground state	End excitations
β	Yes	Yes, possibly gapless	
γ	Yes	Yes	
η	Yes	Yes, possibly gapless	
μ	Yes	Yes, possibly gapless	
τ	Yes	Yes, possibly gapless	
SN	Yes	Yes, possibly gapless	
SC		No, gap < 0.019	Yes
UC		Yes	Yes
AK		Twofold with gap	

(i) η: This is a high field phase (region). As shown in Fig. 6(a), the local magnetization appears incommensurate.

(ii) β: As Γ is made slightly more negative the system transitions from the η phase to the β phase. The local ground-state magnetization along the leg of the ladder, shown in Fig. 6(b), displays a characteristic Möbius form, showing a single twist in S_i^x and S_i^y from one end of the open chain to the other while S_i^z remains constant.

(iii) τ: This phase (region) is adjacent to the β phase, but the beautiful intricate ordering along the leg shown in Fig. 6(c) is clearly distinct from that observed in the β phase with a large variation in S_i^z along the leg. The unit cell for the ordering appears at this value of Γ to be approximately 20 lattice spacings along the ladder leg. At neighboring values of Γ we find similar large unit cell ordering.

(iv) γ: The γ phase is nested in between the SC and β phases occupying a small oval region around $\phi = 0$, $h[111] = 0.5$. The γ phase again shows an exquisite ordering along the ladder leg as shown in Fig. 6(d), in this case with a smaller unit cell of 5 lattice spacings. There is no variation in the ordering throughout the γ phase. The ground state is degenerate and the phase is possibly gapless. However, the bipartite entanglement entropy $S(x)$ is close to constant throughout most of the ladder, which would suggest a gapped phase (see Supplemental Material [77]).

(v) μ: This phase (region) is nested above the SN phase. The magnetic ordering is shown in Fig. 6(e), in this case with a unit cell of 13 lattice spacings along the leg of the ladder. Neighboring values of γ show variations in the local magnetization pattern and it is not clear to what extent this phase is different from the τ phase. There are also variations in the magnetization pattern with $h[111]$ as discussed further in the Supplemental Material [77].

(vi) SN: In zero field the SN was clearly identified. There is no indication of a phase transition as the $h[111]$ is introduced and we therefore assume that the well-defined uniform phase visible in Figs. 4(a) and 4(b) is adiabatically connected to the SN phase in zero field. The phase is gapless and the presence of the nonzero magnetic field induces an incommensurate local magnetization as shown in Fig. 6(f).

As outlined above, the large unit cell ordering occurring in the μ and τ phases (regions) varies with Γ and $h[111]$. The same effect is observed for the incommensurate ordering in the η phase. In fact, the stripes occurring in these phases visible in Fig. 4(a) are likely caused by the variations in the local ordering best compatible with the 24-site unit cell. The lines could therefore represent lock-in transitions.

These phases are therefore not uniform in a conventional sense but could possibly be a series of phases with shifting sizes of unit cells for the magnetic ordering. We have not been able to resolve this.

2. Nonmagnetic phases

We now turn to a discussion of the three remaining disordered phases which do not show any conventional local magnetic ordering apart from that induced by the magnetic field.

(i) SC: In Figs. 7(a) and 7(b) is shown the local magnetization in the SC phase at two different values of ϕ both at $h[111] = 0.38$. In the middle of the chain the local magnetization aligns with the $h[111]$ field and the phase is best described as disordered. Clear excitations at the end of the open chain are visible. As ϕ is increased from -0.08 to -0.10 approaching the μ phase the size of the chain end excitations visibly grows. The SC phase is highly entangled, significantly more so than the AK phase. The ground state does not appear degenerate, but at $h[111] = 0.38$, $\phi = -0.05$ we can limit the gap to the first excited state by $\Delta_1 < 0.019$. The gap is likely smaller in other parts of the phase. The bipartite entanglement entropy $S(x)$ is close to constant throughout most of the ladder, which is also consistent with a gapped phase (see Supplemental Material [77]). The phase shows signs of scalar chiral ordering, as we discuss in more detail below.

(ii) AK: This is the AFM Kitaev phase previously discussed. As shown in In Fig. 7(b) the local magnetization is aligned with the $h[111]$ field and only faint signs of chain end excitations are visible. It is possible to define a string order parameter (SOP) [62] as we discuss below.

(iii) UC: On the left-hand side of the SN phase a new phase appears in the presence of a $h[111]$ field. As we discuss below, this phase has scalar chiral ordering. The ground state is degenerate and the phase is possibly gapless. However, the bipartite entanglement entropy $S(x)$ is close to constant throughout most of the ladder, which would suggest a gapped phase (see Supplemental Material [77]).

3. Total magnetization, $m_\perp$ and $m_\parallel$

It is useful to analyze the total magnetization of the open chain by separating the components parallel $m_\parallel$ and perpendicular $m_\perp$ to the [111] field direction. We define $s^\alpha = \sum_i s_i^\alpha / N$ and then

$$m_\parallel = (s^x + s^y + s^z)/\sqrt{3}. \tag{9}$$

It follows that

$$\vec{m}_\perp = \vec{s} - m_\parallel (1,1,1)/\sqrt{3}. \tag{10}$$

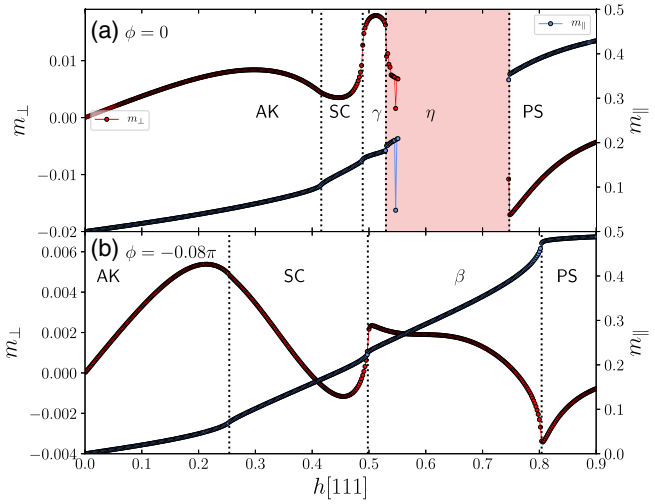

FIG. 8. Magnetization versus field, $h[111]$. (a) $m_\perp$ (red circles) and $m_\parallel$ (blue circles) versus $h[111]$ at the AFM Kitaev point $\phi = 0$. (b) $m_\parallel$ (red circles) and $m_\perp$ (blue circles) versus $h[111]$ (blue circles) near the AFM Kitaev point $\phi = -0.08\pi$. Results in (a) and (b) are from high precision iDMRG calculations with a unit cell of 60 performed at $\phi = -0.08\pi$. The dotted vertical lines denote the transitions at critical fields determined from divergences in χ_h^e and $\chi_h^{\lambda_1}$. Note that $m_\parallel$ is roughly 2 orders of magnitude larger than $m_\perp$.

To facilitate visualization it is most convenient to plot $|m_\perp|$ with a sign that we determine as $\mathrm{sgn}(m_\perp \cdot \hat{a})$ with $\hat{a} = (1, 1, -2)/\sqrt{6}$. Surprisingly, $m_\perp$ is completely aligned or antialigned with $\hat{a}$ for two cases shown in Figs. 8(a) and 8(b). In other words, the angle $m_\perp$ forms with $\hat{a}$ in the $\hat{a}$-$\hat{b}$ plane is either 0 or π. Our results are shown in Figs. 8(a) and 8(b) for $\phi = 0$ and $\phi = -0.08\pi$, respectively. The results are from high precision iDMRG calculations with a unit cell of 60 and a maximal bond dimension of 1000. An important point to notice in Fig. 8 is that $m_\perp$ is 2–3 orders of magnitude smaller than $m_\parallel$.

Let us first discuss the results shown in Fig. 8(a) obtained from a field sweep from 0 to 0.9 at $\phi = 0$. As the η phase is entered, the iDMRG calculations fail to converge and that part of the plot is therefore colored light red. Starting from zero field, $m_\parallel$ (blue circles) is found to approximately linearly increase with $h[111]$ until the SC phase is reached where a kink in $m_\parallel$ is observed, consistent with a divergence of χ_h^e. Through the SC phase $m_\parallel$ increase more rapidly, this phase is therefore "softer," consistent with the large chain end excitations shown in Figs. 7(a) and 7(b). A second kink in $m_\parallel$ is observed as the γ phase is entered, but the increase in $m_\parallel$ throughout the γ phase is less pronounced. As the η phase is entered and excited, kinks in $m_\parallel$ are again observed and in the PS phase the $m_\parallel$ tend toward the fully polarized value of $1/2$. On the other hand, $m_\perp$ (red circles) is nonmonotonic throughout the AK phase, and approaches small values in the SC phase before jumping to larger values in the γ phase. In the polarized state (PS) phase $m_\perp$ changes sign and approaches zero from below.

Our results for a similar field sweep at $\phi = -0.08\pi$ are shown in Fig. 8(b). The position of this field sweep is indicated as the vertical dotted line in Fig. 4(b). Again, $m_\parallel$ is seen to increase more rapidly through the SC and β phases as compared to the AK phase. The phase transitions between the AK, SC, and β phases are clearly visible as kinks in $m_\parallel$ and as the PS phase is approached $m_\parallel$ approach $1/2$ in a characteristic cusp that was not observed between the η and PS phase. The nature of the β-PS transition and η-PS transition therefore clearly appears different. In this case $m_\perp$ is featureless at the AK to SC transition but the SC-β and β-PS transitions are clearly visible. $m_\perp$ changes sign in the SC and β phases. However, $m_\perp$ is in this case 3 orders of magnitude smaller than $m_\parallel$.

For both field sweeps at $\phi = 0$ and $\phi = -0.08\pi$ we emphasize that $m_\perp$ is either aligned or antialigned with $\hat{a}$.

4. Field and angle sweeps

To further investigate the sharpness of the phase transitions occurring in Fig. 4 we have performed high precision sweeps at constant $\phi = -0.08\pi$ and constant $h[111] = 0.15$. The positions of these sweeps are shown as the dotted lines in Fig. 4(b). Our results are shown in Fig. 9 for constant $\phi = -0.08\pi$ and in Fig. 10 for constant $h[111] = 0.15$. In both cases from high precision iDMRG calculations with a unit cell of 60 and a maximal bond dimension of 1000.

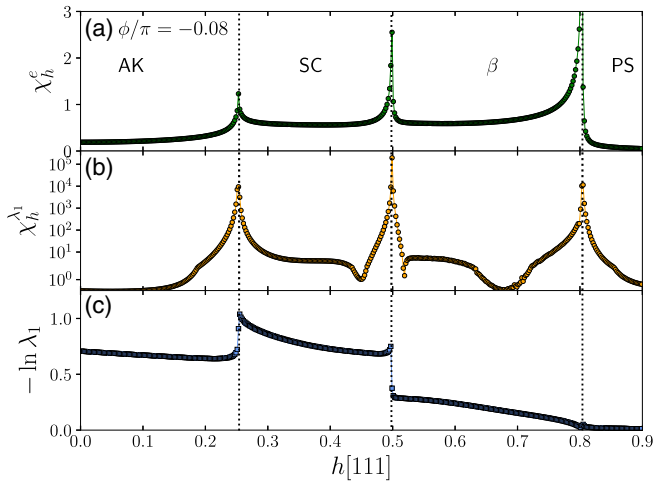

FIG. 9. Field sweep of the phase diagram in the AFM Kitaev region at $\phi = -0.08\pi$. (a) χ_h^e versus $h[111]$. (b) $\chi_h^{\lambda_1}$ versus $h[111]$; note the logarithmic scale. (c) Lowest edge of entanglement spectrum (the single copy entanglement), $-\ln \lambda_1$ from $\rho_{N/2-1}$ versus $h[111]$. All results in (a)–(c) are from high precision iDMRG calculations with a unit cell of 60. The dashed vertical lines correspond to transitions at field values of $h[111]$ of 0.254 (AK-SC), 0.498 (SC-β), and 0.804 (β-PS).

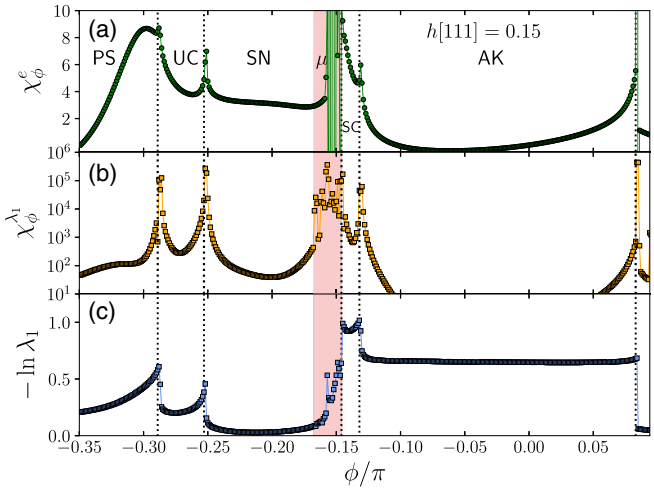

FIG. 10. Angle sweep of the phase diagram in the AFM Kitaev region at $h = 0.15$. (a) χ^e_ϕ versus ϕ/π; note the almost imperceptible divergence in χ^e_ϕ at $\phi = -0.289\pi$. (b) $\chi^{\lambda_1}_\phi$ versus ϕ/π; note the logarithmic scale. (c) Lowest edge of entanglement spectrum (the single copy entanglement), $-\ln\lambda_1$ from $\rho_{N/2-1}$ versus ϕ/π. All results in (a)–(c) are from high precision iDMRG calculations with a unit cell of 60. The dashed vertical lines correspond to transitions at angles ϕ/π of −0.289 (PS-UC), −0.253 (UC-SN), −0.146 (μ-SC), −0.132 (SC-AK), and 0.083 (AK-FM$_{U_6}$). The light red coloring denotes a region of ϕ/π where convergence of the iDMRG is problematic.

Results for a field sweep from $h[111] = 0$ to 0.9 are shown in Fig. 9 for a constant $\phi = -0.08\pi$. In Figs. 9(a)–9(c) we show results for χ^e_h, $\chi^{\lambda_1}_h$, and $-\ln\lambda_1$, respectively. The 3 transitions, AK-SC ($h[111] = 0.254$), SC-β ($h[111] = 0.498$), and β-PS ($h[111] = 0.804$) are very well defined and are in complete agreement between the three different measures. While the β-PS is not all that visible in $-\ln\lambda_1$, it is very clear in $\chi^{\lambda_1}_h$. Five orders of magnitude variation is observed in $\chi^{\lambda_1}_h$.

Results for a ϕ sweep from $\phi = -0.35\pi$ to $\phi = 0.1\pi$ at constant $h[111] = 0.15$ are shown in Fig. 10. In Figs. 10(a)–10(c) we show results for χ^e_h, $\chi^{\lambda_1}_h$, and $-\ln\lambda_1$, respectively. Five transitions are clearly visible. While the PS-UC transition at $\phi = -0.289\pi$ is easy to miss in χ^e_h, it is very well defined in $\chi^{\lambda_1}_h$ and $-\ln\lambda_1$. However, there is a precursor peak in χ^e_h not associated with a transition. The transition SC-AK is clearly defined at $\phi = -0.132\pi$, as the μ phase is approached from the SC side. It is also clear that χ^e_h, $\chi^{\lambda_1}_h$ diverge at the μ-SC transition at $\phi = -0.146\pi$. This transition is therefore well defined. On the other hand, the iDMRG fail to achieve good convergence in the light red colored region, so the transition from SN to μ is not clear. As discussed above it is possible that the μ phase only marks the onset of short-range incommensurate correlations in the SN phase and it is not a distinct phase. It is also possible that improved convergence of the iDMRG would show a divergence in χ^e_h and $\chi^{\lambda_1}_h$ inside the light red colored region.

B. Scalar chirality in the UC and SC phases

The presence of a nonzero Γ term or the magnetic field raises the possibility of chiral ordering. The chirality without magnetic ordering is rare, unless there are three- or four-spin interactions. In 1D system, it was shown that a four-spin interaction produces a long-range scalar chirality [78]. To check the presence of chiral ordering, we label the ith spin on two legs of the ladder as $\mathbf{S}_{i,1}$ and $\mathbf{S}_{i,2}$, where 1 and 2 refer to the bottom leg and top leg, respectively. We then define the scalar chiral order parameter with $\mathbf{S} = \boldsymbol{\sigma}/2$ as follows:

$$\kappa = \langle \sigma_{i,1} \cdot (\sigma_{i,2} \times \sigma_{i+1,1}) \rangle. \tag{11}$$

This clockwise definition is kept for all triangles made of three spins; for example, $\kappa = \langle \sigma_{i,2} \cdot (\sigma_{i+1,2} \times \sigma_{i+1,1}) \rangle$ for upper triangles. If the κ is positive (negative), we assign blue (red) arrows $i \to j \to k$ for $\kappa = \langle \sigma_i \cdot (\sigma_j \times \sigma_k) \rangle$ and all even permutations of i, j, k, which leads to the clockwise (anticlockwise) circulation.

It is also of interest to define the scalar chiral correlation function,

$$C_\kappa(r) = \langle \kappa_i \kappa_{i+r} \rangle, \tag{12}$$

such that $C_\kappa(r) \to \kappa^2$. The scalar chiral order parameter breaks spatial symmetries and time-reversal symmetry, but not SU(2).

In Fig. 11(a) we show κ along a field sweep at constant $\phi = -0.27\pi$ through the UC phase. Results are from high precision iDMRG with a unit cell of 60 sites and a maximal bond dimension of 1000. In this case we determine κ from $C_\kappa(r)$ shown in the inset of Fig. 11(d) at $h[111] = 0.125$. $C_\kappa(r)$ reaches a constant value relatively quickly and κ is clearly nonzero throughout the phase, reaching significant values at the center of the UC phase. The scalar chirality κ is negative throughout the chain and a sketch of the spatial modulation is shown in Fig. 13. Note the edge states appearing on the two opposing legs. Here weaker lines indicate a weaker κ. Since the $h[111]$ field favors alignment of the spins, which would result in $\kappa = 0$, it is rather surprising to observe such a well-defined scalar chirality at finite fields. In Figs. 11(b) and 11(c) are shown χ^e_h and $\chi^{\lambda_1}_h$, respectively. While the transitions delimiting the UC phase are almost absent in χ^e_h, and clearly do not coincide with the broad maximum of χ^e_h around $h[11] \sim 0.25$, they are very well defined in $\chi^{\lambda_1}_h$ and in both cases they coincide with the results for κ in Fig. 11(a). As far as we can tell, the UC phase does not intersect the zero field axis; instead, as can be seen in Fig. 4, the UC and SN phases meet at a triple point close to $\phi = -0.265\pi$. Entanglement close to this

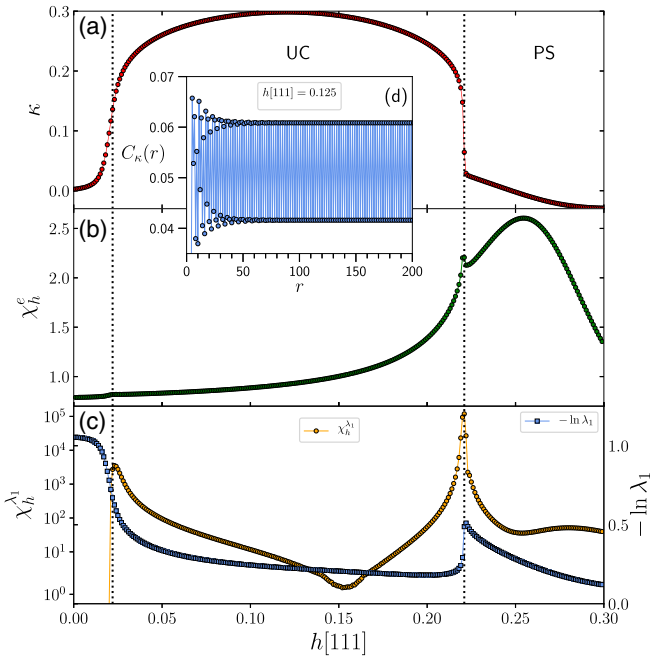

FIG. 11. Ordering in the UC phase. (a) The scalar chirality κ versus $h[111]$. (b) χ^e_h versus $h[111]$. (c) $\chi^{\lambda_1}_h$ (orange circles) and $-\ln\lambda_1$ (blue circles) versus $h[111]$. (d) The chiral correlation function $C(r)$ along the ladder at $h[111] = 0.125$. All results in (a)–(d) are from high precision iDMRG calculations with a unit cell of 60 performed at $\phi = -0.27\pi$. The dotted vertical lines denote the transitions at critical fields $h^c_1 = 0.022$ and $h^c_2 = 0.221$. Note that the divergence in χ^e_h at h^c_1 is imperceptible and very small at h^c_2 where it occurs away from the maximum. However, $\chi^{\lambda_1}_\phi$ show very well defined peaks at both h^c_1 and h^c_2.

triple point is therefore very elevated, which is why $-\ln\lambda_1$ [blue squares in Fig. 11(c)] is so high close to zero field.

In Fig. 12 we show iDMRG calculations for κ versus $h[111]$ at a fixed $\phi = -0.08$, crossing the AK, SC, and β phases. χ^e_h and $\chi^{\lambda_1}_h$ along the same line in the phase diagram are shown in Fig. 9. As before, κ is obtained from calculations of $C_\kappa(r)$ in the large r limit and the sign of κ from local direct estimates of κ. In this case there is a spatial $+-$ alternation of κ as shown in Fig. 14, but the magnitude of κ is the same for each triangle leading to the zero flux in the system. Although there is weak chirality in the AK and β phases, κ is an order of magnitude larger in the SC phase and jumps rather abruptly at the critical points indicated by the dotted lines in Fig. 12. In Fig. 12(b) is shown $C_\kappa(r)$ versus r at $h[111] = 0.42$ which attain a constant value for modest values of $r \sim 20$. Figure 12(c) shows the bipartite entanglement obtained from a bipartition of the system at site r. The resulting entanglement entropy $S(r) = -\mathrm{Tr}\rho_r \ln\rho_r$ is shown versus r for a finite ladder with $N = 400$ and OBC. Clearly, $S(r)$ is close to constant in the middle of the ladder, which would be consistent with the existence of a nonzero gap in the SC phase (see also Supplemental Material [77]).

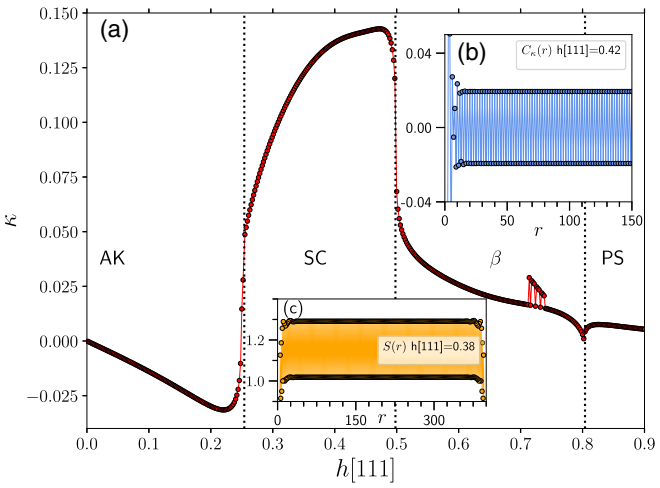

FIG. 12. Ordering along $\phi = -0.08\pi$ (AK, SC, and β phase). (a) The scalar chirality κ versus $h[111]$. (b) The chiral correlation function $C(r)$ along the ladder at $h[111] = 0.42$. (c) Bipartite entanglement entropy $S(r)$ versus r at $h[111] = 0.38$. Results in (a) and (b) are from high precision iDMRG calculations with a unit cell of 60 performed at $\phi = -0.08\pi$ while (c) is from finite-size DMRG with OBC at $\phi = -0.08\pi$, $h[111] = 0.38$. The dotted vertical lines denote the transitions at critical fields $h^c_1 = 0.254$, $h^c_2 = 0.498$, and $h^c_3 = 0.804$.

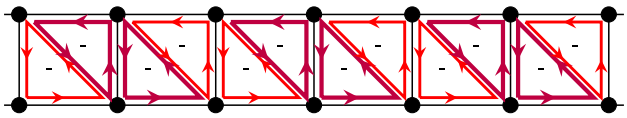

FIG. 13. Scalar chirality in the UC phase. At $h = 0.125$ and $\phi = -0.27$, $\kappa = -0.204$, -0.298, -0.298, -0.204 for first four triangles, respectively, and then repeat.

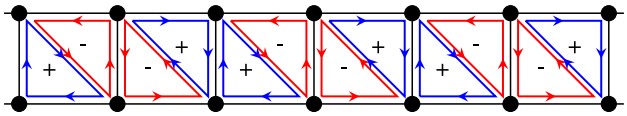

FIG. 14. Scalar chirality in the SC phase. At $h = 0.42$ and $\phi = -0.08$, $\kappa = 0.139$, -0.139, -0.139, 0.139 for first four triangles, respectively, and then repeat.

To make a comparison to the AK phase, we also compute the chirality in the AK phase, and its pattern is shown in Fig. 15. κ has distinctly different circulations. It has a staggering circulation between upper and lower triangles,

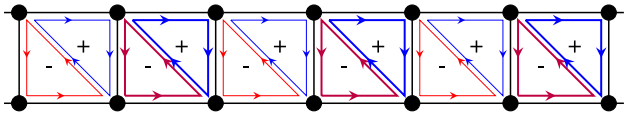

FIG. 15. Scalar chirality in the AK phase. At $h = 0.2$ and $\phi = -0.08$, $\kappa = -0.0191$, 0.0191, -0.0466, 0.0466 for first four triangles, respectively, and then repeat.

but different staggering from the SC phase. For both the AK and SC phases, the magnitude of κ is the same for all pairs of triangles, implying that there is zero-net flux in the system. The phase transition from the AK to SC phases is accompanied by the sharp change of both magnitude and distinct pattern of κ.

C. String order and mapping to KQ model

Through a *nonlocal* unitary transformation it is possible to map the KG ladder to a Heisenberg model with four spin interactions that we shall call the KQ model. The starting point is a *nonlocal* unitary transformation V introduced in Ref. [62] for an N-site chain with OBC:

$$V = \prod_{\substack{j+1<k \\ j \text{ odd}, k \text{ odd} \\ j=1,\ldots,N-3 \\ k=3,\ldots,N-1}} U(j,k), \tag{13}$$

with the individual $U(j,k)$ given as follows:

$$U(j,k) = e^{i\pi(S^y_j + S^y_{j+1})\cdot(S^x_k + S^x_{k+1})}. \tag{14}$$

At the AFM Kitaev point, $\phi = 0$, V maps the ladder with open boundary conditions to a so-called dangling-Z model, H_{d-Z}, that has long-range ordering in $\langle \tilde{S}^z_i \tilde{S}^z_{i+r} \rangle$, where $\tilde{S}$ are the spins in H_{d-Z} [62]. If this correlation function is transformed back to the original Kitaev ladder, one arrives at a string correlation function of the following form:

$$\langle \mathcal{O}^z(r) \rangle = 4\langle \tilde{S}^z_2 \tilde{S}^z_{2+r} \rangle = (-1)^{\lfloor (r+1)/2 \rfloor} \times \begin{cases} \left\langle \sigma^y_1 \sigma^x_2 \left(\prod_{k=3}^{r} \sigma^z_k \right) \sigma^x_{r+1} \sigma^y_{r+2} \right\rangle & r \text{ even} \\ \left\langle \sigma^y_1 \sigma^x_2 \left(\prod_{k=3}^{r+1} \sigma^z_k \right) \sigma^y_{r+2} \sigma^x_{r+3} \right\rangle & r \text{ odd}. \end{cases} \tag{15}$$

Note that in Ref. [62] some of the indices in Eq. (15) in the expression for r even were incorrect. With this definition we find that the usual plaquette operator [1] $W_p \equiv \mathcal{O}^z(r=4)$. W_p is often used to characterize the AK phase. See Supplemental Material [77].

Results for $\mathcal{O}^z$ are shown in Fig. 16. In the presence of a nonzero magnetic field or a nonzero Γ the string order correlation function $\mathcal{O}^z(r)$ is not long-range. Instead, as shown in the inset in Fig. 16(a) for $h[111] = 0.25$, it decays exponentially to zero. However, the length scale describing this exponential decay is extremely large, often exceeding hundreds or, for small enough Γ, $h[111]$, thousands of lattice spacings. The extent of the AK phase can therefore be determined by determining $\mathcal{O}^z(r=100)$ or $\mathcal{O}^z(r=900)$, which remain nonzero throughout the AK phase. This is illustrated in Fig. 16(a) where both $\mathcal{O}^z(r=100)$ (solid blue triangles) and $\mathcal{O}^z(r=900)$ (solid green circles) are plotted versus $h[111]$ alongside χ^e_h (open red circles) at $\phi = 0$. Clearly, $\mathcal{O}^z(r=100)$ drops abruptly toward zero at the phase transition between AK and the SC phase. Figure 16(b) shows $\mathcal{O}^z(r=100)$ versus ϕ at fixed $h[111] = 0.15$, where abrupt changes in $\mathcal{O}^z(r=100)$ are observed at the boundary of the AK phase.

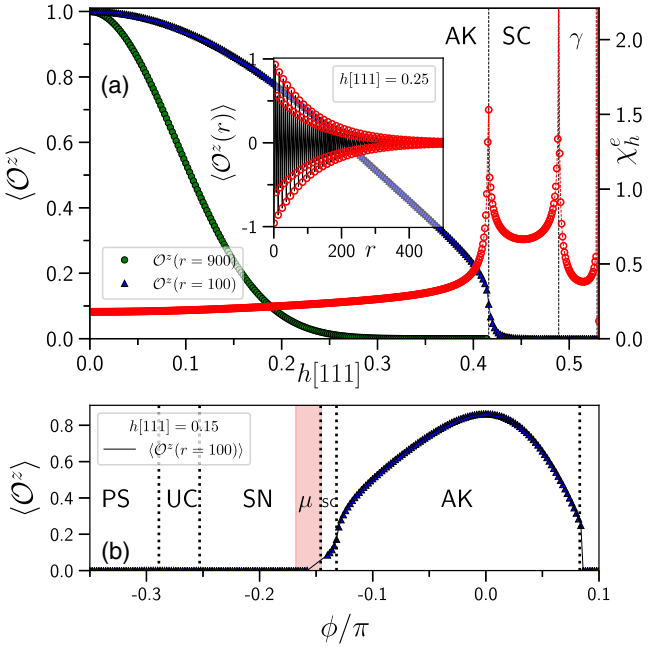

FIG. 16. String order $\langle \mathcal{O}^z \rangle$ versus field in the AFM Kitaev region. (a) $\langle \mathcal{O}^z(r=100) \rangle$ (blue triangles) and $\langle \mathcal{O}^z(r=100) \rangle$ (green circles) versus $h[111]$ at the AFM Kitaev point $\phi = 0$ shown along with χ^e_h. Open red circles show χ^e_h. The inset shows $\langle O^z(r) \rangle$ (red circles) versus r at $h[111] = 0.25$, $\phi = 0$. (b) $\langle \mathcal{O}^z(r=100) \rangle$ (blue triangles) versus ϕ/π at fixed $h[111] = 0.15$. Results in (a) and (b) are from high precision iDMRG calculations with a unit cell of 60. The dotted vertical lines denote the transitions at critical fields determined from divergences in χ^e_h and $\chi^{\lambda_1}_h$.

1. Mapping to KQ model

It is of considerable interest to explore nonlocal unitary operators that will lead to string order correlation functions showing long-range order also for $\Gamma \neq 0$. We begin by considering how the ladder is transformed under the U_6 transformation previously described. If the spins on one leg of the ladder are numbered $i = 1 \ldots N/2$ we assign them a second label $k = (i-1) \bmod 6 + 1$, and on the second leg we assign the label $k = (i+2) \bmod 6 + 1$. With this labeling we introduce the following notation for the transformed bonds:

$$\begin{aligned} x' &: -KS^x_i S^x_j - \Gamma(S^y_i S^y_j + S^z_i S^z_j), \\ y' &: -KS^y_i S^y_j - \Gamma(S^x_i S^x_j + S^z_i S^z_j), \\ z' &: -KS^z_i S^z_j - \Gamma(S^x_i S^x_j + S^y_i S^y_j). \end{aligned} \tag{16}$$

Here j is a nearest neighbor site. With this notation we can represent the transformed ladder using the picture in Fig. 17.

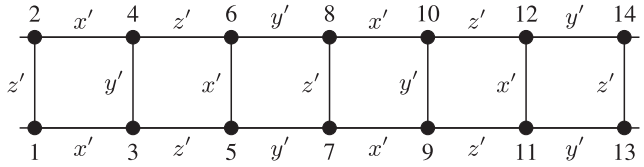

FIG. 17. The KG ladder after the U_6 local transformation.

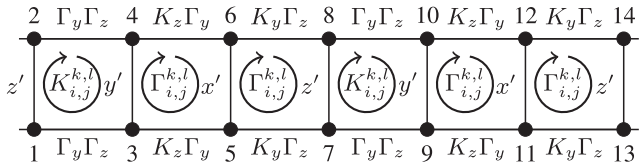

FIG. 18. H_{KQ}. The KG ladder after the U_6 transformation followed by the W transformation.

We then consider the zero-field case with OBC and change notation slightly compared to Ref. [62] by using an equivalent *nonlocal* unitary operator:

$$W = \prod_{\substack{j+1<k \\ j \text{ odd}, k \text{ odd} \\ j=1,\ldots,N-3 \\ k=3,\ldots,N-1}} w(j,k), \tag{17}$$

with the individual $w(j,k)$ given as follows:

$$w(j,k) = e^{i\pi(S^y_j + S^y_{j+1})\cdot(S^z_k + S^z_{k+1})}, \tag{18}$$

and $W^\dagger = W$. With this definition of W we see that on the vertical bonds of the ladder W leaves all interactions unchanged:

$$WS^\alpha_1 S^\alpha_2 W = S^\alpha_1 S^\alpha_2, \qquad WS^\alpha_3 S^\alpha_4 W = S^\alpha_3 S^\alpha_4, \ldots. \tag{19}$$

However, on horizontal bonds we find

$$WS^y_2 S^y_4 W = -S^y_1 S^y_4, \qquad WS^y_3 S^y_5 W = -S^y_4 S^y_5, \ldots. \tag{20}$$

Note that W effectively *moves* the bond and changes the sign of the interaction. Likewise, we get for the horizontal zz bonds

$$VS^z_2 S^z_4 V = -S^z_2 S^z_3, \qquad VS^z_3 S^z_5 V = -S^z_3 S^z_6, \ldots. \tag{21}$$

However, the horizontal xx bonds give rise to nontrivial four-spin interactions. Specifically,

$$VS^x_2 S^x_4 V = -\sigma^y_1 S^z_2 \sigma^z_3 S^y_4, \qquad VS^x_3 S^x_5 V = -S^z_3 \sigma^y_4 S^y_5 \sigma^z_6, \ldots, \tag{22}$$

thereby coupling the four spins around a plaquette. We then introduce additional notation for transformed bonds:

$$\begin{aligned} K_z\Gamma_y &: KS^z_i S^z_j + \Gamma S^y_i S^y_j, \\ K_y\Gamma_z &: KS^y_i S^y_j + \Gamma S^z_i S^z_j, \\ \Gamma_y\Gamma_z &: \Gamma S^y_i S^y_j + \Gamma S^z_i S^z_j, \\ \Gamma^{k,l}_{i,j} &: 4\Gamma(S^z_k S^z_l S^y_i S^y_j + S^y_k S^y_l S^z_i S^z_j), \\ K^{k,l}_{i,j} &: 4K(S^z_k S^z_l S^y_i S^y_j + S^y_k S^y_l S^z_i S^z_j). \end{aligned} \tag{23}$$

With this notation in hand we can now apply the W transformation to the U_6 transformed ladder shown in Fig. 17. The resulting Hamiltonian can be drawn in the manner shown in Fig. 18. It is quite remarkable that the W transformation has generated four-spin exchange terms. We call this H_{KQ} Hamiltonian the KQ ladder since the model is a close cousin of JQ models [57] extensively studied as models of deconfined criticality [58]. Unexpectedly, the ground state for the KQ model in the AK phase has a significant overlap with a rung-triplet state. If we define

$$\begin{aligned} t_x &= (|\uparrow\uparrow\rangle - |\downarrow\downarrow\rangle)/\sqrt{2}, \\ t_y &= (|\uparrow\uparrow\rangle + |\downarrow\downarrow\rangle)/\sqrt{2}, \\ t_z &= (|\uparrow\downarrow\rangle + |\downarrow\uparrow\rangle)/\sqrt{2}, \end{aligned} \tag{24}$$

then we can pictorially draw the rung-triplet state as shown in Fig. 19. With OBC there is another energetically equivalent rung-triplet state obtained by translation as shown in Fig. 19. The two states approximates the doublet ground state of the KQ model. Surprisingly, the unit cell for these triplet states is 12 sites and not six sites as one might have expected from the structure of H_{KG}. Ordering of this type has previously been studied using SOPs inspired by the studies of $s = 1$ spin chains. If $\tau^\alpha_i = S^\alpha_{i,1} + S^\alpha_{i+1,2}$ are the sum of two diagonally situated spins, one defines [79,80]

$$\mathcal{O}^\alpha_{\mathrm{even}}(r) = -\left\langle \tau^\alpha_i \exp\left(i\pi \sum_{l=i+1}^{i+r-1} \tau^\alpha_l\right) \tau^\alpha_{i+r} \right\rangle. \tag{25}$$

This order parameter has been used to distinguish topologically distinct phases in Heisenberg ladders and is nonzero in the rung-singlet phase where the topological number is even.

In Fig. 20 we show results for $\mathcal{O}^z_{\mathrm{even}}$ estimated from $\mathcal{O}^z_{\mathrm{even}}(r)$ in the large r limit on systems with $N = 120$ and

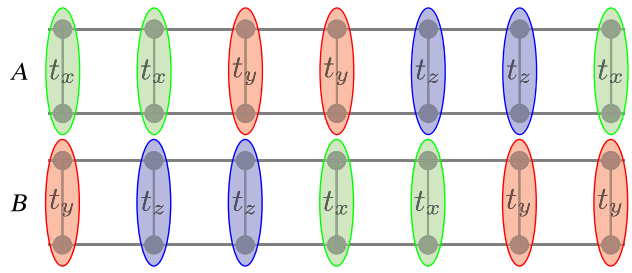

FIG. 19. The rung-triplet states A and B for the KQ model.

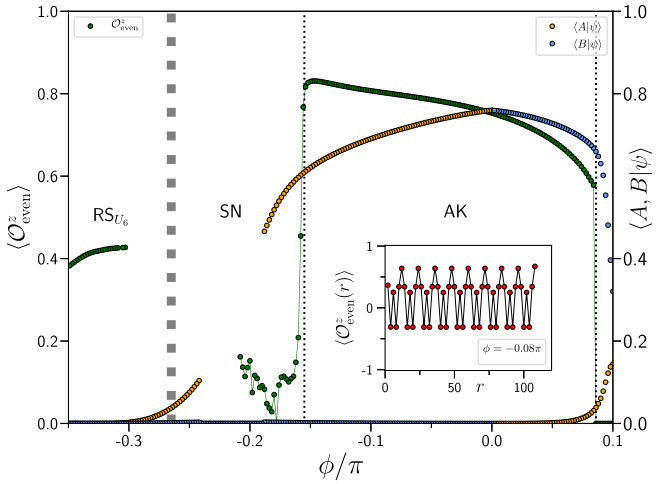

FIG. 20. String order parameter $\langle \mathcal{O}^z_{\rm even} \rangle$ versus field (green circles) in the AFM Kitaev region for $H_{\rm KQ}$ with $N = 120$. Results are shown alongside the overlaps $\langle A|\psi\rangle$ and $\langle B|\psi\rangle$ from calculations with $N = 12$. Results are from high precision DMRG calculations with OBC. The dotted vertical lines denote the transitions at critical fields determined from divergences in χ^e_h and $\chi^{\lambda_1}_h$. An example of $\mathcal{O}^z_{\rm even}(r)$ at $\phi = -0.08\pi$ is shown in the inset.

OBC. An example of $\mathcal{O}^z_{\rm even}(r)$ at $\phi = 0.08\pi$ is plotted in the inset of Fig. 20. This SOP drops abruptly to zero at the limits of the AK phase and, as can be seen from the inset, there is no exponential decay observed in $\mathcal{O}^z_{\rm even}(r)$ which instead quickly attains a constant value. As expected, $\mathcal{O}^z_{\rm even}$ is also nonzero in the RS$_{U_6}$ phase, but clearly zero in the SN phase. Also shown in Fig. 20 are the overlaps with the rung-triplet states $\langle A|\psi\rangle$ and $\langle B|\psi\rangle$ as obtained from small $N = 12$ systems with OBC. There are significant finite-size effects at the boundaries of the AK phase for the overlaps; although they drop to zero outside the AK phase, the critical points are not as well defined as for $\mathcal{O}^z_{\rm even}$. The rung-triplet states shown in Fig. 20 are approximate and for $N > 12$ different linear combinations enter such that with the simple definitions of the rung-triplet states above $\langle A|\psi\rangle$ and $\langle B|\psi\rangle$ tend to zero as $N \to \infty$. However, $\mathcal{O}^z_{\rm even}$ is clearly nonzero in the AK phase and in the KQ model this phase is therefore topologically equivalent to the Haldane-like phases observed in Heisenberg ladders with even topological number. Since the KQ model is related to the KG model through unitary transformations, the same must be true for the KG ladder throughout the AK phase. Calculations in the FK phase show that $\mathcal{O}^z_{\rm even}$ is also clearly nonzero in zero field throughout that phase but drops to zero in the AΓ phase.

VI. COMPARISON: THE HONEYCOMB KG MODEL

It is important to note that the pure AFM Kitaev under the magnetic field studied by DMRG and 24-site ED exhibits an intermediate gapless phase before it polarizes. A U(1) spin liquid was suggested for this field-induced gapless phase [45]. However, in the two-leg ladder, we found *five* distinct phases including AK, SC, γ, η, and PS at the pure AFM Kitaev point (white thin line at $\phi = 0$ in Fig. 4), as the magnetic field increases. There are several factors including the obvious geometry difference that may result in the different results between the 24-site honeycomb cluster and current results. To understand possible origins of the difference, we investigate the following systems at AFM Kitaev point, $\phi = 0$.

First we study the 24-site ladder using ED and compare the result with iDMRG with a unit cell of 60, to understand the finite-size effects. The results of χ^e_h are shown in Fig. 21(a), where the red and green dots are obtained by iDMRG and ED, respectively. Note that, due to problems with convergence, there are no iDMRG results in the η phase. The sharp transitions seen in the iDMRG between AK and SC at $h[111] = 0.416$, and between SC and γ at $h[111] = 0.489$, are replaced by broad bumps in ED, while the transition between γ and η at $h[111] = 0.530$ in the iDMRG is also sharp in the ED results. The transition to the PS phase occurs around the same field strength for both ED and iDMRG, $h[111] = 0.747$. There are a couple of sharp features within η phase only found in ED, which we assign to finite-size effects. Other than these additional peaks in η phase, the results are remarkably similar.

We also investigate the 24-site C_3 symmetric honeycomb cluster using the ED. χ^e_h is shown in Fig. 21(b), where h sweeps from 0 to 0.8 by $\delta h = 0.001$, much smaller steps than previous studies [45]. There are four transitions found at $h[111] = 0.388$, 0.543, 0.598, and 0.641, which may suggest three intermediate phases. For comparison Ref. [45] only finds 2 transitions performing ED on the same 24-site C_3 cluster, presumably due to a larger δh. However, based on the finite-size effects found in 24-site ladder ED, we suspect that there are significant finite-size effects in this system that makes it hard to determine whether these phases correspond to the SC, γ, and η phases, or only one (SC) or two phases survive in the thermodynamic limit. Indeed when the field is tilted away from the c axis, there are only two transitions found in the 24-site C_3 cluster [45], while the three intermediate phases—SC, γ, and η—found in the iDMRG ladder persist even in the tilted field (see Appendix B). Given that γ and η are incommensurate magnetic phases, and thus sensitive to the shape of cluster, we speculate that they likely turn into another type of incommensurate phase confined in the C_3 symmetric cluster. The chirality of the SC phase may survive in the honeycomb cluster defined at a triangle made of nearest neighbors or next nearest neighbors of honeycomb lattice. This is an excellent topic for future study, as it requires a bigger size system to check the chiral correlation $C(r)$.

To shed further light on the occurrence of gapless excitations in 24-site C_3 cluster in ED, we choose an even

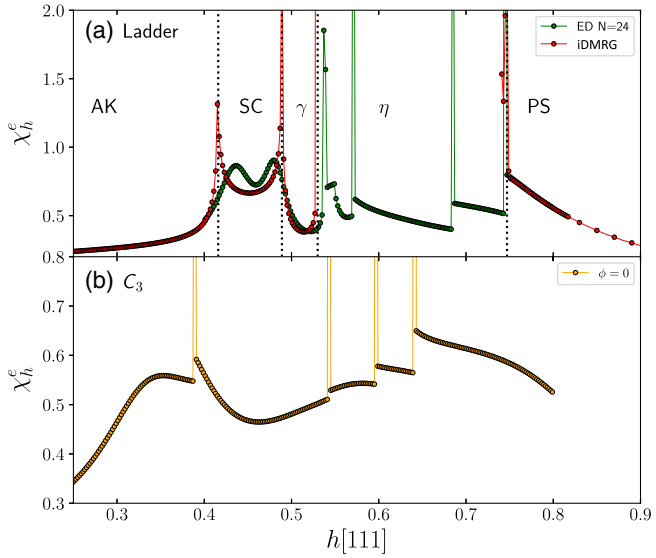

FIG. 21. Comparison between the two-leg ladder and the 24-site C_3 symmetric honeycomb geometry at $\phi = 0$. (a) The ladder. χ_h^e versus $h[111]$ as obtained from ED with $N = 24$ (green circles) and from high precision iDMRG with a unit cell of 60 (red circles). (b) The C_3 symmetric honeycomb geometry. χ_h^e versus $h[111]$ as obtained from ED with $N = 24$ (orange circles). The critical fields are at 0.388, 0.543, 0.598, and 0.641.

smaller cluster of 2×6 ladder, and compute various quantities under the [111] field. The energy spectrum is shown in Fig. 22, which indicates three phase transitions (red dashed lines obtained from χ_h^e with four phases: the low-field Kitaev phase changes to a field-induced intermediate phase, which then transitions to another intermediate phase, before it becomes the polarized state). The collapse of the excitations is remarkably similar to 24-site C_3 cluster, suggesting that the intermediate gapless excitation feature is insensitive to the cluster size and shape, even though the critical fields where such phases arise change depending on the shape. The qualitative behavior is

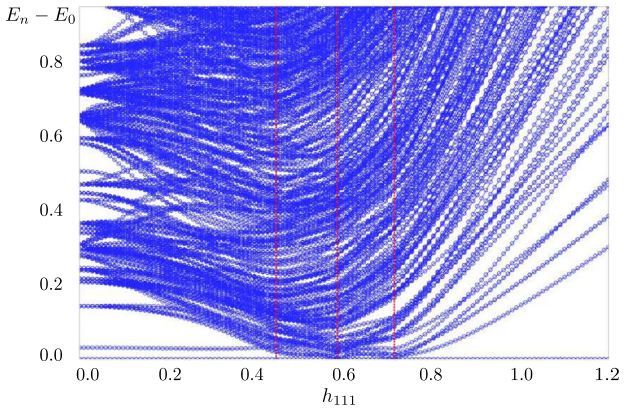

FIG. 22. The energy spectrum of the pure AFM Kitaev limit under the [111] field using 2×6 ladder.

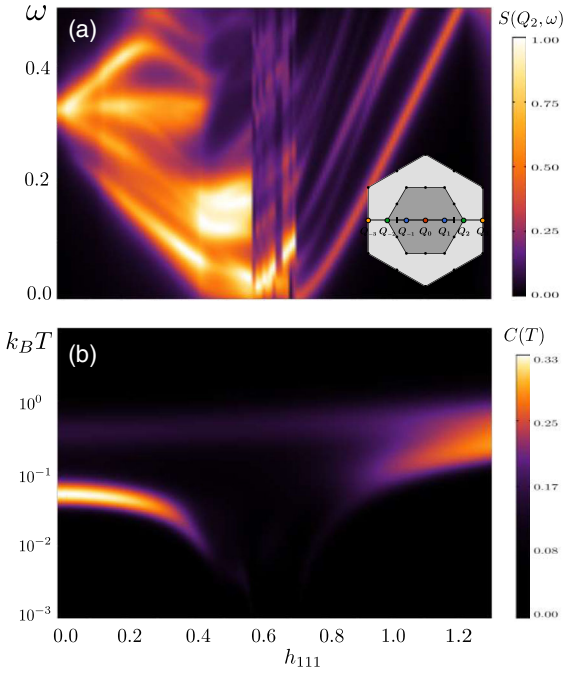

FIG. 23. (a) Dynamical spin structure factor $S(Q_2, \omega)$ at the wave vector of Q_2 defined in the BZ figure shown in the inset and (b) specific heat $C(T)$ of the pure AFM Kitaev limit under the [111] field using 2×6 ladder.

similar to the 24-site ladder and C_3 ED presented above. However, it is not clear if there is one or two intermediate phases, as the incommensurability of γ and η phases would suffer from the change of cluster size and shape, as discussed above. The dynamical structure factor at a particular momentum Q_2 (shown in the inset) and the specific heat in the field are shown in Figs. 23(a) and 23(b), respectively. The first intermediate phase is likely disordered, while the second intermediate phase likely exhibits incommensurate ordering. They do not exhibit well-defined excitation spectra in the specific heat similar to what is observed in the C_3 24-site ED [45]. While it is a 12-sites ladder geometry, the qualitative results are incredibly similar to the DMRG phase diagram at the $\phi = 0$ AFM Kitaev point under the field and the 24-site C_3 symmetric honeycomb geometry results [45]. It shows a dense energy spectrum in the intermediate states of both disordered (SC) and field-induced incommensurate (η or γ) phase.

The above analysis with small ladder and C_3 cluster suggests that the AFM Kitaev 2D honeycomb model under the field may also display a richer phase diagram than what has been reported, and a high resolution numerical calculation is required to refine the phase diagram. Since the γ or η phases also show a dense energy spectrum, it is important to differentiate the U(1) spin liquid from the incommensurate phases in the honeycomb AFM Kitaev limit. Comparing the critical field above which gapless spin liquid occurs in 24-site ED [45], it is likely that the

disordered SC phase with enhanced entanglement and edge excitations extends to the gapless spin liquid in the honeycomb lattice, and the incommensurate phase is mixed with a polarized state, which was missed in 24-site ED of the honeycomb lattice. We conclude that the ladder model at the AFM Kitaev limit captures both disordered and incommensurate magnetically ordered phases under the magnetic field, and offers future directions in searching for a spin liquid in the honeycomb KG model.

VII. SUMMARY AND DISCUSSION

The KG model consists of two bond-dependent interactions, namely the Kitaev and Gamma interactions. The Kitaev interaction on the honeycomb lattice exhibits a spin liquid with fractionalized excitations. In particular, under a time-reversal symmetry breaking term, the excitations obey non-Abelian statistics. The Gamma interaction is another highly frustrated interaction leading to a macroscopic degeneracy in the classical limit, and quantum fluctuations do not lift the degeneracy found in the AFM classical Gamma model [81].

Since these two frustrating interactions are dominant interactions in realistic descriptions of emerging Kitaev candidates such as $RuCl_3$, the minimal KG model was initially proposed to understand $RuCl_3$ [49,82]. The magnetic field has been a crucial parameter, as the system may undergo a transition into a field-induced disordered phase before the trivial PS appears. Aside from its relevance to Kitaev materials, the minimal KG model may offer a playground to discover exotic spin liquids due to the combined frustration of the K and Gamma term, and thus has been extensively studied for the past few years. Given the huge phase space of AFM and FM Kitaev, AFM and FM Gamma, and the field, most studies are limited to a narrow phase space focusing on the FM Kitaev and AFM Kitaev regions. Many numerical methods have been used to identify phases of the extended Kitaev model under the field and intriguing results were reported near AFM Kitaev and FM Kitaev regions including the field-induced gapless U(1) spin liquid near the AFM Kitaev region [45]. However, it is not clear if the gapless excitations are due to more conventional physics such as incommensurate ordering.

Here we investigate the entire phase space of the KG *ladder* model under the magnetic field. While the geometry is limited to the ladder, it has the great advantage of allowing for high numerical precision such as accessing iDMRG with a high precision mode with a unit cell of 60 and a maximal bond dimension of 1000. Numerical calculations are therefore very well controlled. We found an extremely rich phase diagram of the KG model under the field. Among 15 distinct phases identified, nine phases appear near the AFM Kitaev region alone. In the zero field, there is a quadrupole ordered phase named SN, two magnetically ordered phases (FM_{U_6} and RS_{U_6}) straightforward to understand from the mapping of six-site transformation, and the disordered AK phase. It is interesting that the SN phase found in the KG chain [63] survives in the ladder. Other than the AK phase (which becomes the Kitaev spin liquid in the 2D limit), the zero-field phases are ordered and the entanglement entropy is rather low. Under the field, highly entangled phases emerge. Apart from several incommensurate magnetic ordered phases, two highly entangled phases denoted by SC referring staggered chirality and UC uniform chirality are induced by the field. These phases exhibit distinct chirality orderings and high entanglement entropy with gapless edge excitations when the boundary is open.

The ladder results presented here offer several important insights in possible spin liquids and not-yet-identified phases in the 2D honeycomb lattice. We would like to recall that the pure Kitaev model in the ladder corresponding to AK and FK in this study is gapped, where the ladder can be viewed as a coupled chain [83]. As the number of chains grows, the ground state changes between gapped and gapless depending on the even and odd numbers of the chains, and eventually maps to the 2D Kitaev spin liquid in a true 2D limit. The AK and FK are gapped due to the geometry of the ladder, but its nature, magnetically disordered with high entanglement, is captured in the ladder model. Applying similar logic, we suggest that the disordered SC phase is related to the spin liquid in the 2D limit. The SC phase has a staggered chirality but different patterns from the AK phase in field, which differentiate the two phases. While it is gapped in the ladder, it may become gapless as the number of chains grows.

Interestingly the previous DMRG studies on the pure AFM Kitaev point ($\phi = 0$) under the $[111]$ field with 3–5 number of legs reported different central charge in the intermediate phase. For three-leg chains, the central charge $c = 1$ [50] was reported, while for four- and five-leg chains, $c = 0$ [50] and $c \sim 4$ [39], respectively, were found. Based on the central charge arguments, these studies indicate that there are gapless excitations associated with a spinon Fermi surface in the intermediate field region. It was suggested that the spinon Fermi surface pockets are around the K/K' and Γ point of the first Brillouin zone [50], while the other DMRG study proposed the pockets around M and Γ points [52]. The existence of a spinon Fermi surface in momentum space is yet to be determined.

While most of the previous studies reported the field-induced intermediate phase as a single phase at the pure AFM Kitaev $\phi = 0$ point in the $[111]$ field [37,40,41,45,50,52], a separation of the intermediate region into three phases was noted in Ref. [39], and the middle phase, which corresponds to the γ phase in the ladder, grows in extent with larger bond dimensions where five legs were used. We find three different intermediate phases, SC, γ, and η, in the ladder at $\phi = 0$. While the γ phase occupies a tiny phase

space in the ladder, it is possible that this gapless incommensurate γ extends its phase space, as the number of chains grows. This implies that the chiral spin-liquid candidate SC may require a finite FM Γ interaction, as it generates more frustration. The SC phase with long-range chirality and enhanced entanglement appearing at the intermediate field region of the ladder likely evolves to a field-induced spin liquid with a finite *staggered chirality*.

The UC phase is another candidate of spin liquid. It has uniform chirality pattern with high entanglement with a finite net flux, and it appears at very low field between SN and six-site transformed FM phase. This phase space has not been well explored in honeycomb clusters, and we suggest further studies in this region to look for a possible spin liquid. The nature of the SC and UC phases and statistics of excitations in these phases are excellent topics for future study. A study of the evolution of each phase region under an added Heisenberg interaction would also be an interesting task left for the future.

Possible incommensurate orderings in the 2D limit also deserve some discussion. Incommensurate orderings are generally difficult to pin down, as they depend on the size of cluster, and the ordering wave vector itself changes even inside a phase due to the nature of incommensuration. In the ladder, we found several incommensurate orderings. Some have high entanglement indicating a quantum order coexisting with an incommensurate ordering. The possibility of incommensurate ordering has been excluded in the C_3 symmetric cluster, mainly because of technical difficulty set by a limited size. Our ladder study suggests several incommensurate orderings may be present in the 2D honeycomb lattice, and future studies on such a possibility on larger honeycomb clusters are desirable.

ACKNOWLEDGMENTS

We give special thanks to M. Gohlke for pointing out a magnetic order in the SN phase, and also thank W. Yang, A. Nocera, Y. B. Kim, and C. Hickey for useful discussions. E. S. acknowledges support from the NSERC Discovery Grant No. 05759-2017. A. C., J. S. G., and H. Y. K. acknowledge support from the NSERC Discovery Grant No. 06089-2016. H. Y. K. acknowledges support from CIFAR and the Canada Research Chairs Program. Computations were performed in part on the GPC and Niagara supercomputers at the SciNet HPC Consortium. SciNet is funded by the Canada Foundation for Innovation under the auspices of Compute Canada, the Government of Ontario, Ontario Research Fund—Research Excellence, and the University of Toronto. Computations were also performed in part by support provided by SHARCNET [84] and Compute/Calcul Canada [85]. Part of the numerical calculations were performed using the ITensor library [86].

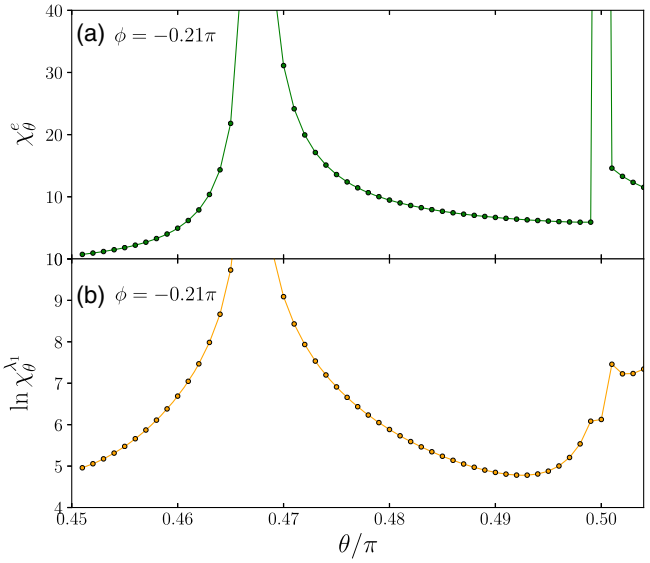

FIG. 24. (a) χ^e_θ and (b) $\ln\chi^{\lambda_1}_\theta$ versus θ at a fixed $\phi = -0.21\pi$ inside the SN phase where we set $J \equiv K\cos\theta$ for the KG ladder. It shows a clear first order transition at $J = 0$ indicating a first order transition point. Results are from high precision iDMRG with unit cell of 60.

APPENDIX A: SN PHASE AT ZERO FIELD

To understand the zero-field SN phase where the DMRG with OBC finds two different magnetic orderings depending on the system, we introduce an additional Heisenberg coupling, $J = K\cos\theta$, and study (a) the energy susceptibility χ^e_θ and (b) $\ln\chi^{\lambda_1}_\theta$ versus θ at a fixed $\phi = -0.21\pi$. This is to check if there is a first order transition as a function of J occurring along the line of the SN. Indeed a clear first order transition is found in the energy susceptibility at $\theta = \pi/2$, i.e., $J = 0$ as shown in Fig. 24. We conclude that the phase space denoted by the SN is a line of first order transitions separating two different magnetic ordering states. Since the nematic (spin-quadropole) order is finite in both ordered states, we keep the name the SN for this line of first order transitions, throughout the paper.

APPENDIX B: AFM KITAEV POINT IN TILTED FIELD

It is an interesting question if the phases found around the AFM Kitaev point persist when the field direction is changed. In order to investigate this we have calculated χ^e_h in the presence of a field tilted slightly away from the [111] direction toward the $[11-2]$ direction of the following form: $\cos(\theta)h[111] + \sin(\theta)h[11-2]$ with $\theta = 7.5°$. Our results, obtained from iDMRG, are shown in Fig. 25. In Fig. 25(a) we show for comparison our previous results for $\theta = 0$, and in Fig. 25(b) for a tilted field with $\theta = 7.5°$. The AK, SC, and γ phases are still

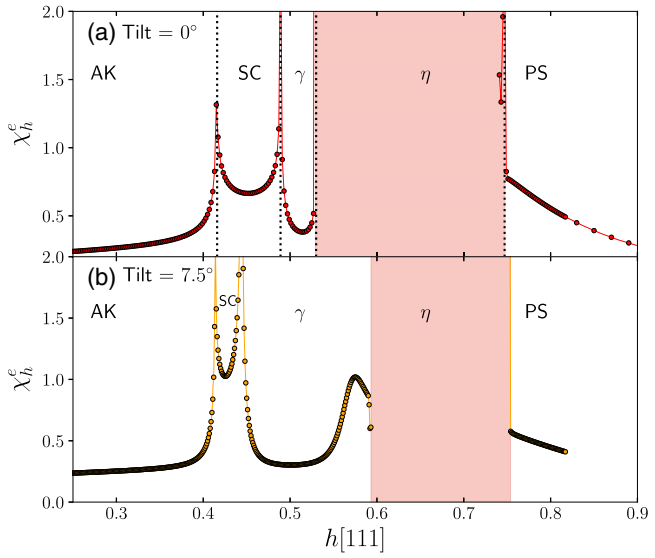

FIG. 25. χ_h^e versus field for the KG ladder for (a) $h[111]$ field and (b) a field $\cos(\theta)h[111] + \sin(\theta)h[11-2]$ with $\theta = 7.5°$. The light red shading indicates regions where the iDMRG does not converge well. Results are from high precision iDMRG with unit cell of 60.

clearly present, as is the transition to the polarized phase PS. However, the transition to the η phase is in this case less well defined. In both panels the light red coloring indicates regions where the iDMRG does not converge well. Remarkably the critical fields for the AK-SC and η-PS transition appear almost unchanged by the tilt of the field.

[1] A. Y. Kitaev, *Anyons in an Exactly Solved Model and Beyond*, Ann. Phys. (Amsterdam) **321**, 2 (2006).

[2] G. Khaliullin, *Orbital Order and Fluctuations in Mott Insulators*, Prog. Theor. Phys. Suppl. **160**, 155 (2005).

[3] G. Jackeli and G. Khaliullin, *Mott Insulators in the Strong Spin-Orbit Coupling Limit: From Heisenberg to a Quantum Compass and Kitaev Models*, Phys. Rev. Lett. **102**, 017205 (2009).

[4] J. G. Rau, E. K.-H. Lee, and H.-Y. Kee, *Generic Spin Model for the Honeycomb Iridates beyond the Kitaev Limit*, Phys. Rev. Lett. **112**, 077204 (2014).

[5] K. W. Plumb, J. P. Clancy, L. J. Sandilands, V. V. Shankar, Y. F. Hu, K. S. Burch, H.-Y. Kee, and Y.-J. Kim, α-$RuCl_3$*: A Spin-Orbit Assisted Mott Insulator on a Honeycomb Lattice*, Phys. Rev. B **90**, 041112(R) (2014).

[6] H.-S. Kim, V. Vijay Shankar, A. Catuneanu, and H.-Y. Kee, *Kitaev Magnetism in Honeycomb* α-$RuCl_3$ *with Intermediate Spin-Orbit Coupling*, Phys. Rev. B **91**, 241110(R) (2015).

[7] A. Koitzsch, C. Habenicht, E. Müller, M. Knupfer, B. Büchner, H. C. Kandpal, J. van den Brink, D. Nowak, A. Isaeva, and T. Doert, J_{eff} *Description of the Honeycomb Mott Insulator* α-$RuCl_3$, Phys. Rev. Lett. **117**, 126403 (2016).

[8] L. J. Sandilands, Y. Tian, A. A. Reijnders, H.-S. Kim, K. W. Plumb, Y. J. Kim, H.-Y. Kee, and K. S. Burch, *Spin-Orbit Excitations and Electronic Structure of the Putative Kitaev Magnet* α-$RuCl_3$, Phys. Rev. B **93**, 075144 (2016).

[9] X. Zhou, H. Li, J. A. Waugh, S. Parham, H.-S. Kim, J. A. Sears, A. Gomes, H.-Y. Kee, Y.-J. Kim, and D. S. Dessau, *Angle-Resolved Photoemission Study of the Kitaev Candidate* α-$RuCl_3$, Phys. Rev. B **94**, 161106(R) (2016).

[10] A. Banerjee, C. A. Bridges, J.-Q. Yan, A. A. Aczel, L. Li, M. B. Stone, G. E. Granroth, M. D. Lumsden, Y. Yiu, J. Knolle, S. Bhattacharjee, D. L. Kovrizhin, R. Moessner, D. A. Tennant, D. G. Mandrus, and S. E. Nagler, *Proximate Kitaev Quantum Spin Liquid Behaviour in a Honeycomb Magnet*, Nat. Mater. **15**, 733 (2016).

[11] H.-S. Kim and H.-Y. Kee, *Crystal Structure and Magnetism in* α-$RuCl_3$*: An Ab Initio Study*, Phys. Rev. B **93**, 155143 (2016).

[12] L. Janssen, E. C. Andrade, and M. Vojta, *Magnetization Processes of Zigzag States on the Honeycomb Lattice: Identifying Spin Models for* α-$RuCl_3$ *and* Na_2IrO_3, Phys. Rev. B **96**, 064430 (2017).

[13] S. M. Winter, Y. Li, H. O. Jeschke, and R. Valentí, *Challenges in Design of Kitaev Materials: Magnetic Interactions from Competing Energy Scales*, Phys. Rev. B **93**, 214431 (2016).

[14] J. G. Rau, E. K.-H. Lee, and H.-Y. Kee, *Spin-Orbit Physics Giving Rise to Novel Phases in Correlated Systems: Iridates and Related Materials*, Annu. Rev. Condens. Matter Phys. **7**, 195 (2016).

[15] S. M. Winter, A. A. Tsirlin, M. Daghofer, J. van den Brink, Y. Singh, P. Gegenwart, and R. Valentí, *Models and Materials for Generalized Kitaev Magnetism*, J. Phys. Condens. Matter **29**, 493002 (2017).

[16] M. Hermanns, I. Kimchi, and J. Knolle, *Physics of the Kitaev Model: Fractionalization, Dynamic Correlations, and Material Connections*, Annu. Rev. Condens. Matter Phys. **9**, 17 (2018).

[17] H. Takagi, T. Takayama, G. Jackeli, G. Khaliullin, and S. E. Nagler, *Concept and Realization of Kitaev Quantum Spin Liquids*, Nat. Rev. Phys. **1**, 264 (2019).

[18] L. Janssen and M. Vojta, *Heisenberg-Kitaev Physics in Magnetic Fields*, J. Phys. Condens. Matter **31**, 423002 (2019).

[19] L. J. Sandilands, Y. Tian, K. W. Plumb, Y.-J. Kim, and K. S. Burch, *Scattering Continuum and Possible Fractionalized Excitations in* α-$RuCl_3$, Phys. Rev. Lett. **114**, 147201 (2015).

[20] Y. Kasahara, T. Ohnishi, Y. Mizukami, O. Tanaka, S. Ma, K. Sugii, N. Kurita, H. Tanaka, J. Nasu, Y. Motome, T. Shibauchi, and Y. Matsuda, *Majorana Quantization and Half-Integer Thermal Quantum Hall Effect in a Kitaev Spin Liquid*, Nature (London) **559**, 227 (2018).

[21] R. D. Johnson, S. C. Williams, A. A. Haghighirad, J. Singleton, V. Zapf, P. Manuel, I. I. Mazin, Y. Li, H. O. Jeschke, R. Valentí, and R. Coldea, *Monoclinic Crystal Structure of* α-$RuCl_3$ *and the Zigzag Antiferromagnetic Ground State*, Phys. Rev. B **92**, 235119 (2015).

[22] S.-H. Baek, S.-H. Do, K.-Y. Choi, Y. S. Kwon, A. U. B. Wolter, S. Nishimoto, J. van den Brink, and B. Büchner, *Evidence for a Field-Induced Quantum Spin Liquid in* α-$RuCl_3$, Phys. Rev. Lett. **119**, 037201 (2017).

[23] J. Zheng, K. Ran, T. Li, J. Wang, P. Wang, B. Liu, Z.-X. Liu, B. Normand, J. Wen, and W. Yu, *Gapless Spin Excitations in the Field-Induced Quantum Spin Liquid Phase of* α-$RuCl_3$, Phys. Rev. Lett. **119**, 227208 (2017).

[24] I. A. Leahy, C. A. Pocs, P. E. Siegfried, D. Graf, S.-H. Do, K.-Y. Choi, B. Normand, and M. Lee, *Anomalous Thermal Conductivity and Magnetic Torque Response in the Honeycomb Magnet* α-$RuCl_3$, Phys. Rev. Lett. **118**, 187203 (2017).

[25] R. Hentrich, A. U. B. Wolter, X. Zotos, W. Brenig, D. Nowak, A. Isaeva, T. Doert, A. Banerjee, P. Lampen-Kelley, D. G. Mandrus, S. E. Nagler, J. Sears, Y.-J. Kim, B. Büchner, and C. Hess, *Unusual Phonon Heat Transport in* α-$RuCl_3$*: Strong Spin-Phonon Scattering and Field-Induced Spin Gap*, Phys. Rev. Lett. **120**, 117204 (2018).

[26] P. Lampen-Kelley, L. Janssen, E. C. Andrade, S. Rachel, J. Q. Yan, C. Balz, D. G. Mandrus, S. E. Nagler, and M. Vojta, *Field-Induced Intermediate Phase in* α-$RuCl_3$*: Non-Coplanar Order, Phase Diagram, and Proximate Spin Liquid*, arXiv:1807.06192.

[27] N. Janša, A. Zorko, M. Gomilšek, M. Pregelj, K. W. Krämer, D. Biner, A. Biffin, C. Rüegg, and M. Klanjšek, *Observation of Two Types of Fractional Excitation in the Kitaev Honeycomb Magnet*, Nat. Phys. **14**, 786 (2018).

[28] A. Banerjee, P. Lampen-Kelley, J. Knolle, C. Balz, A. A. Aczel, B. Winn, Y. Liu, D. Pajerowski, J. Yan, C. A. Bridges, A. T. Savici, B. C. Chakoumakos, M. D. Lumsden, D. A. Tennant, R. Moessner, D. G. Mandrus, and S. E. Nagler, *Excitations in the Field-Induced Quantum Spin Liquid State of* α-$RuCl_3$, npj Quantum Mater. **3**, 8 (2018).

[29] L. Y. Shi, Y. Q. Liu, T. Lin, M. Y. Zhang, S. J. Zhang, L. Wang, Y. G. Shi, T. Dong, and N. L. Wang, *Field-Induced Magnon Excitation and In-Gap Absorption in the Kitaev Candidate* $RuCl_3$, Phys. Rev. B **98**, 094414 (2018).

[30] S. Widmann, V. Tsurkan, D. A. Prishchenko, V. G. Mazurenko, A. A. Tsirlin, and A. Loidl, *Thermodynamic Evidence of Fractionalized Excitations in* α-$RuCl_3$, Phys. Rev. B **99**, 094415 (2019).

[31] A. Sahasrabudhe, D. A. S. Kaib, S. Reschke, R. German, T. C. Koethe, J. Buhot, D. Kamenskyi, C. Hickey, P. Becker, V. Tsurkan, A. Loidl, S. H. Do, K. Y. Choi, M. Grüninger, S. M. Winter, Z. Wang, R. Valentí, and P. H. M. van Loosdrecht, *High-Field Quantum Disordered State in* α-$RuCl_3$*: Spin Flips, Bound States, and Multiparticle Continuum*, Phys. Rev. B **101**, 140410(R) (2020).

[32] A. U. B. Wolter, L. T. Corredor, L. Janssen, K. Nenkov, S. Schönecker, S.-H. Do, K.-Y. Choi, R. Albrecht, J. Hunger, T. Doert, M. Vojta, and B. Büchner, *Field-Induced Quantum Criticality in the Kitaev System* α-$RuCl_3$, Phys. Rev. B **96**, 041405(R) (2017).

[33] Y. J. Yu, Y. Xu, K. J. Ran, J. M. Ni, Y. Y. Huang, J. H. Wang, J. S. Wen, and S. Y. Li, *Ultralow-Temperature Thermal Conductivity of the Kitaev Honeycomb Magnet* α-$RuCl_3$ *across the Field-Induced Phase Transition*, Phys. Rev. Lett. **120**, 067202 (2018).

[34] M. Yamashita, N. Kurita, and H. Tanaka, *Sample Dependence of the Half-Integer Quantized Thermal Hall Effect in a Kitaev Candidate* α-$RuCl_3$, arXiv:2005.00798.

[35] R. Yadav, N. A. Bogdanov, V. M. Katukuri, S. Nishimoto, J. Van Den Brink, and L. Hozoi, *Kitaev Exchange and Field-Induced Quantum Spin-Liquid States in Honeycomb* α-$RuCl_3$, Sci. Rep. **6**, 37925 (2016).

[36] G.-W. Chern, Y. Sizyuk, C. Price, and N. B. Perkins, *Kitaev-Heisenberg Model in a Magnetic Field: Order-by-Disorder and Commensurate-Incommensurate Transitions*, Phys. Rev. B **95**, 144427 (2017).

[37] Z. Zhu, I. Kimchi, D. N. Sheng, and L. Fu, *Robust Non-Abelian Spin Liquid and a Possible Intermediate Phase in the Antiferromagnetic Kitaev Model with Magnetic Field*, Phys. Rev. B **97**, 241110(R) (2018).

[38] S. Liang, B.-S. He, Z.-Y. Dong, W. Chen, J.-X. Li, and Q.-H. Wang, *Response and Phase Transition of a Kitaev Spin Liquid in a Local Magnetic Field*, Phys. Rev. B **98**, 104410 (2018).

[39] M. Gohlke, R. Moessner, and F. Pollmann, *Dynamical and Topological Properties of the Kitaev Model in a [111] Magnetic Field*, Phys. Rev. B **98**, 014418 (2018).

[40] J. Nasu, Y. Kato, Y. Kamiya, and Y. Motome, *Successive Majorana Topological Transitions Driven by a Magnetic Field in the Kitaev Model*, Phys. Rev. B **98**, 060416(R) (2018).

[41] D. C. Ronquillo, A. Vengal, and N. Trivedi, *Signatures of Magnetic-Field-Driven Quantum Phase Transitions in the Entanglement Entropy and Spin Dynamics of the kitaev Honeycomb Model*, Phys. Rev. B **99**, 140413(R) (2019).

[42] S. Liang, M.-H. Jiang, W. Chen, J.-X. Li, and Q.-H. Wang, *Intermediate Gapless Phase and Topological Phase Transition of the Kitaev Model in a Uniform Magnetic Field*, Phys. Rev. B **98**, 054433 (2018).

[43] Z.-X. Liu and B. Normand, *Dirac and Chiral Quantum Spin Liquids on the Honeycomb Lattice in a Magnetic Field*, Phys. Rev. Lett. **120**, 187201 (2018).

[44] D. A. S. Kaib, S. M. Winter, and R. Valentí, *Kitaev Honeycomb Models in Magnetic Fields: Dynamical Response and Dual Models*, Phys. Rev. B **100**, 144445 (2019).

[45] C. Hickey and S. Trebst, *Gapless Visons and Emergent U(1) Spin Liquid in the Kitaev Honeycomb Model: Complete Phase Diagram in Tilted Magnetic Fields*, Nat. Commun. **10**, 530 (2019).

[46] L. E. Chern, R. Kaneko, H.-Y. Lee, and Y. B. Kim, *Magnetic Field Induced Competing Phases in Spin-Orbital Entangled Kitaev Magnets*, Phys. Rev. Research **2**, 013014 (2020).

[47] H.-Y. Lee, R. Kaneko, L. E. Chern, T. Okubo, Y. Yamaji, N. Kawashima, and Y. B. Kim, *Magnetic Field Induced Quantum Phases in a Tensor Network Study of Kitaev Magnets*, Nat. Commun. **11**, 1639 (2020).

[48] M. Gohlke, L. E. Chern, H.-Y. Kee, and Y. B. Kim, *Emergence of a Nematic Paramagnet via Quantum Order-by-Disorder and Pseudo-Goldstone Modes in Kitaev Magnets*, Phys. Rev. Research **2**, 043023 (2020).

[49] J. S. Gordon, A. Catuneanu, E. S. Sørensen, and H.-Y. Kee, *Theory of the Field-Revealed Kitaev Spin Liquid*, Nat. Commun. **10**, 2470 (2019).

[50] H.-C. Jiang, C.-Y. Wang, B. Huang, and Y.-M. Lu, *Field Induced Quantum Spin Liquid with Spinon Fermi Surfaces in the Kitaev Model*, arXiv:1809.08247.

[51] L. Zou and Y.-C. He, *Field-Induced* QCD_3*-Chern-Simons Quantum Criticalities in Kitaev Materials*, Phys. Rev. Research **2**, 013072 (2020).

[52] N. D. Patel and N. Trivedi, *Magnetic Field-Induced Intermediate Quantum Spin Liquid with a Spinon Fermi Surface*, Proc. Natl. Acad. Sci. U.S.A. **116**, 12199 (2019).

[53] J. c. v. Chaloupka and G. Khaliullin, *Hidden Symmetries of the Extended Kitaev-Heisenberg Model: Implications for the Honeycomb-Lattice Iridates* A_2IrO_3, Phys. Rev. B **92**, 024413 (2015).

[54] I. Kimchi and R. Coldea, *Spin Dynamics of Counterrotating Kitaev Spirals via Duality*, Phys. Rev. B **94**, 201110(R) (2016).

[55] I. Rousochatzakis and N. B. Perkins, *Magnetic Field Induced Evolution of Intertwined Orders in the Kitaev Magnet* β-Li_2IrO_3, Phys. Rev. B **97**, 174423 (2018).

[56] P. P. Stavropoulos, A. Catuneanu, and H.-Y. Kee, *Counterrotating Spiral Order in Three-Dimensional Iridates: Signature of Hidden Symmetry in the Kitaev-*Γ *Model*, Phys. Rev. B **98**, 104401 (2018).

[57] A. W. Sandvik, *Evidence for Deconfined Quantum Criticality in a Two-Dimensional Heisenberg Model with Four-Spin Interactions*, Phys. Rev. Lett. **98**, 227202 (2007).

[58] T. Senthil, A. Vishwanath, L. Balents, S. Sachdev, and M. P. A. Fisher, *Deconfined Quantum Critical Points*, Science **303**, 1490 (2004).

[59] W. Yang, A. Nocera, T. Tummuru, H.-Y. Kee, and I. Affleck, *Phase Diagram of the Spin-*$1/2$ *Kitaev-Gamma Chain and Emergent Su(2) Symmetry*, Phys. Rev. Lett. **124**, 147205 (2020).

[60] G. Karakonstantakis, L. Liu, R. Thomale, and S. A. Kivelson, *Correlations and Renormalization of the Electron-Phonon Coupling in the Honeycomb Hubbard Ladder and Superconductivity in Polyacene*, Phys. Rev. B **88**, 224512 (2013).

[61] X.-Y. Feng, G.-M. Zhang, and T. Xiang, *Topological Characterization of Quantum Phase Transitions in a Spin-*$1/2$ *Model*, Phys. Rev. Lett. **98**, 087204 (2007).

[62] A. Catuneanu, E. S. Sørensen, and H.-Y. Kee, *Nonlocal String Order Parameter in the* $s = \frac{1}{2}$ *Kitaev-Heisenberg Ladder*, Phys. Rev. B **99**, 195112 (2019).

[63] W. Yang, A. Nocera, E. S. Sørensen, H.-Y. Kee, and I. Affleck, *Phase Diagram of the Spin-*$1/2$ *Kitaev-Gamma Chain and Emergent Su(2) Symmetry*, arXiv:2004.06074.

[64] S. R. White and R. M. Noack, *Real-Space Quantum Renormalization Groups*, Phys. Rev. Lett. **68**, 3487 (1992).

[65] S. R. White, *Density Matrix Formulation for Quantum Renormalization Groups*, Phys. Rev. Lett. **69**, 2863 (1992).

[66] S. R. White, *Density-Matrix Algorithms for Quantum Renormalization Groups*, Phys. Rev. B **48**, 10345 (1993).

[67] U. Schollwöck, *The Density-Matrix Renormalization Group*, Rev. Mod. Phys. **77**, 259 (2005).

[68] K. A. Hallberg, *New Trends in Density Matrix Renormalization*, Adv. Phys. **55**, 477 (2006).

[69] U. Schollwöck, *The Density-Matrix Renormalization Group in the Age of Matrix Product States*, Ann. Phys. (Amsterdam) **326**, 96 (2011), Special Issue.

[70] I. P. McCulloch, *Infinite Size Density Matrix Renormalization Group, Revisited*, arXiv:0804.2509.

[71] A. F. Albuquerque, F. Alet, C. Sire, and S. Capponi, *Quantum Critical Scaling of Fidelity Susceptibility*, Phys. Rev. B **81**, 064418 (2010).

[72] H. Li and F. D. M. Haldane, *Entanglement Spectrum as a Generalization of Entanglement Entropy: Identification of Topological Order in Non-Abelian Fractional Quantum Hall Effect States*, Phys. Rev. Lett. **101**, 010504 (2008).

[73] J. Eisert and M. Cramer, *Single-Copy Entanglement in Critical Quantum Spin Chains*, Phys. Rev. A **72**, 042112 (2005).

[74] A. Catuneanu, *Magnetic and Topological Aspects of Spin Liquid Candidates with Strong Spin-Orbit Coupling*, Ph.D thesis, University of Toronto, 2019.

[75] E. Dagotto, J. Riera, and D. Scalapino, *Superconductivity in Ladders and Coupled Planes*, Phys. Rev. B **45**, 5744 (1992).

[76] T. Barnes, E. Dagotto, J. Riera, and E. S. Swanson, *Excitation Spectrum of Heisenberg Spin Ladders*, Phys. Rev. B **47**, 3196 (1993).

[77] See Supplemental Material at http://link.aps.org/supplemental/10.1103/PhysRevX.11.011013 for additional data in support of the AFM Kitaev region phase diagram.

[78] A. Läuchli, G. Schmid, and M. Troyer, *Phase Diagram of a Spin Ladder with Cyclic Four-Spin Exchange*, Phys. Rev. B **67**, 100409(R) (2003).

[79] E. H. Kim, G. Fáth, J. Sólyom, and D. J. Scalapino, *Phase Transitions between Topologically Distinct Gapped Phases in Isotropic Spin Ladders*, Phys. Rev. B **62**, 14965 (2000).

[80] G. Fáth, O. Ligeza, and J. Sólyom, *String Order in Spin Liquid Phases of Spin Ladders*, Phys. Rev. B **63**, 134403 (2001).

[81] I. Rousochatzakis and N. B. Perkins, *Classical Spin Liquid Instability Driven by Off-Diagonal Exchange in Strong Spin-Orbit Magnets*, Phys. Rev. Lett. **118**, 147204 (2017).

[82] A. Catuneanu, Y. Yamaji, G. Wachtel, Y. B. Kim, and H.-Y. Kee, *Path to Stable Quantum Spin Liquids in Spin-Orbit Coupled Correlated Materials*, npj Quantum Mater. **3**, 23 (2018).

[83] X.-Y. Feng, G.-M. Zhang, and T. Xiang, *Topological Characterization of Quantum Phase Transitions in a Spin-*$1/2$ *Model*, Phys. Rev. Lett. **98**, 087204 (2007).

[84] https://www.sharcnet.ca.

[85] https://www.computecanada.ca.

[86] M. Fishman, S. R. White, and E. Miles Stoudenmire, *The ITensor Software Library for Tensor Network Calculations*, arXiv:2007.14822.